

# A gradient-based framework for maximizing mixing in binary fluids

M.F. Eggl<sup>1</sup>, P.J. Schmid

*Department of Mathematics, Imperial College London, London SW7 2AZ, United Kingdom*

---

## Abstract

A computational framework based on nonlinear direct-adjoint looping is presented for optimizing mixing strategies for binary fluid systems. The governing equations are the nonlinear Navier-Stokes equations, augmented by an evolution equation for a passive scalar, which are solved by a spectral Fourier-based method. The stirrers are embedded in the computational domain by a Brinkman-penalization technique, and shape and path gradients for the stirrers are computed from the adjoint solution. Four cases of increasing complexity are considered, which demonstrate the efficiency and effectiveness of the computational approach and algorithm. Significant improvements in mixing efficiency, within the externally imposed bounds, are achieved in all cases.

*Keywords:* mixing, optimization, penalization, adjoint method

---

## 1. Introduction

The mixing of binary fluid is a problem of fundamental concern in fluids dynamics, as its mechanisms play an important role in a wide variety of industrial fields and in many fluid processes encountered in daily life. The spreading and mixing of pollutants in the ocean [1], the ventilation of a building [2, 3], the mixing of air and fuel for subsequent combustion [4] or the mixing in microfluidic devices [5, 6] are but a few examples where mixing processes play an important role. The food processing, pharmaceutical and consumer-product industry are further sectors where an improvement of mixing efficiency would translate into immediate profits as well as a more consistent quality of the end product.

Mixing in industrial applications is often accomplished by stirrers, i.e., moving bodies of a given shape embedded in a mixing vessel whose task it is to produce long filaments [7] which are subsequently diffused. This two-step process, which is principally at the core of binary fluid mixing by stirrers, has been recognized as a fundamental mechanism and has been studied extensively to gain insight and to guide control strategies. We will consider the case of stirrer-induced mixing and its optimization in this article.

From a computational point of view, one of the difficulties of stirrer-based mixing stems from the treatment of the fluid-structure interaction between the embedded, moving stirrers and the binary fluid. Various options exist and have been pursued by previous studies, such as body-fitted meshes [8] or the method of fictitious domains [9]. These techniques are, however, often restricted to simpler configurations or are excessively costly due to the need to remesh at each time step

---

<sup>1</sup>Corresponding author: maximilian.egg11@imperial.ac.uk

(after the solid object has been advanced). An attractive alternative to the above methods is the penalization method which will be adopted in this article. Introduced in reference [10], solutions obtained by the penalization method have been rigorously shown to converge to the corresponding solution of the Navier Stokes equation [11] for the respective complex domain. Supporting studies, including an asymptotic analysis, are summarized in [12], and applications to high Mach-number flows [13] and turbulent flow past cylinders [14], among many other examples, have demonstrated the effectiveness and flexibility of the approach. A penalization approach has also been taken by [15], coupled with a level-set technique to express the geometry, and applied by [16] to optimize the shape of actuators. The appeal of the penalization method lies in its simple derivation and straightforward numerical implementation.

A further complication of the mixing problem is the nonlinear nature of its underlying governing equations. Optimizing stirring strategies using a gradient-based approach, as will be pursued in this article, will have to deal with the solution of nonlinear equations and the checkpointing problem for the dual/adjoint problem (see details below). The complexity of the flow does not furnish equilibrium points about which to linearize, not even over a limited horizon of validity. Instead, the full nonlinear problem has to be tackled, and nonlinear adjoint looping techniques [17] have to be employed for the stirrer geometry and/or stirrer path.

Rather than investigating merely the effects and mechanisms of mixing, several previous studies have attempted the control and optimization of mixing processes. These include, among others, optimal control of mixing via entropy maximization of a flow governed by two orthogonal shear flows [18], and optimal mixing of a steady Stokes flow by optimizing the mix-norm [19, 20]. A concise review of measuring mixing as well as mixing optimization is given in [21] as well as in [22].

We wish to blend the advantages of a penalization method for describing the motion of stirrers through the binary fluid with the direct-adjoint methodology for gradient-based optimization. The challenges of this approach lie in the extraction of path-derivatives and shape-derivatives from the forward-backward integration of the direct and dual problem (the Karush-Kuhn-Tucker system). The full computational framework inherits the flexibility, efficiency and accuracy of the fluid-structure treatment by penalization and the effective convergence of the PDE-constrained optimization method to reach a minimum in mixing variance (or any other mixing norm), and thus a better mixed state of the binary system.

The test cases and their underlying geometry, namely a circular dish with one or more embedded rotating stirrers, are taken with a view towards industrial configurations, where cylindrical mixing containers with rotating stirrers are commonplace [23]. Within this setup the algorithm can prove its mettle and provide significant improvements in mixing efficiency.

The rest of this article is organized in the following manner. In section § 2 we present the governing equations of the system we wish to analyze as well as an in-depth review of the penalization method incorporated into these equations. In section § 3 we then turn our attention to the numerical algorithm and implementation, covering the discretization of the system and introducing a formulation that is particular amenable to deriving the dual/adjoint system. We then present, in section § 4, the methodology and algorithm used to achieve optimality. This includes the introduction of an augmented Lagrangian of the system and the derivation of the optimality system (KKT-system), with special emphasis on the penalization notion established earlier. Furthermore, we also present a step-by-step summary of the optimal-mixing algorithm. Lastly, in section § 5, we demonstrate the efficacy of the algorithm by presenting test cases of progressing complexity. These test cases have been chosen to probe and assess the convergence and optimization behavior of the algorithm, and results range from simple (and anticipated) to more difficult (and less intuitive).

They are meant to gain experience with the optimization strategy, which in turn will guide future efforts and more complex setups. Conclusions are offered in section 6. The appendices will provide details on various derivations in the text.

## 2. Governing equations and general assumptions

### 2.1. Governing equations

We will consider mixing processes of a binary, miscible fluid in a parameter regime where inertial effect cannot be ignored, yet turbulent fluid motion has not developed. In addition, we assume for simplicity that both liquids behave as Newtonian fluids. This parameter regime is commonly observed in a wide range of industrial applications and shall serve here as a basis for establishing a mathematical and computational framework for the optimization of mixing efficiency.

The underlying equations governing the motion of the fluid is then given by the incompressible Navier-Stokes equations which read in primitive form

$$\partial_t \mathbf{u} + \mathbf{u} \cdot \nabla \mathbf{u} + \nabla p - Re^{-1} \nabla^2 \mathbf{u} = 0, \quad (1a)$$

$$\nabla \cdot \mathbf{u} = 0 \quad (1b)$$

with  $\mathbf{u}$  as the velocity vector and  $p$  as the pressure field. The equations have been stated in non-dimensional form, where appropriate characteristic length ( $L_0$ ) and velocity ( $u_0$ ) scales have been chosen to render the equations dimensionless. This introduces the Reynolds number  $Re$  based on these characteristic scales, i.e.,  $Re = \frac{u_0 L_0}{\nu}$  with  $\nu$  as the kinematic viscosity.

The above equations have to be augmented by a scalar field, denoted by  $\theta$ , to describe the mixing process. This is accomplished by considering

$$\partial_t \theta + \mathbf{u} \cdot \nabla \theta - Pe^{-1} \nabla^2 \theta = 0 \quad (2)$$

as the evolution equation that transports  $\theta$ , where  $\theta$  is defined between 0 and 1. This advection-diffusion equation for the passive scalar is parameterized by the Péclet number  $Pe$ , defined as  $Pe = \frac{u_0 L_0}{\kappa}$ , with  $u_0$  and  $L_0$  again as the characteristic velocity and length scales, respectively, and  $\kappa$  denoting the diffusion coefficient of the mixing fluid.

As mentioned above, we target the parameter regime beyond Stokes mixing, where inertial effects become relevant, but below the onset of turbulence, where mixing by turbulent fluctuations dominates. To this end, we consider the parameter setting  $Re = Pe = 1000$ , which represents inertial, yet laminar flow. In this regime, we retain two important physical mixing processes: advection and diffusion. The complex interplay between these two mechanisms shall be the focus of our analysis and the target of our optimization algorithm; advection in a generated shear field will be exploited to produce small-scale structures, which are subsequently subjected to diffusion and mixing [20].

### 2.2. Measuring mixedness

In anticipation of our stated goal of enhancing mixing efficiency, we have to introduce a measure that quantifies the degree of mixedness of a particular configuration. This measure shall be based solely on the passive scalar field  $\theta$ .

In general, mixing is defined as the reduction of inhomogeneities of a given indicator field [24], which still leaves open a precise mathematical definition to be used in our framework. Several norms of the passive scalar  $\theta$  that attempt to mathematically define the measure of mixedness have been proposed and used in the past [25], among them the variance or the more complex negative-index and fractional-index Sobolev norms [26].

As the choice of norm may influence the outcome of the optimization, but will not affect the design of our computational optimization platform, we will focus, for simplicity, on the variance norm of the passive scalar  $\theta$ . This rather intuitive measure attains higher values for an unmixed field (with high levels of inhomogeneities) and decreases as the scalar field  $\theta$  becomes more mixed. Mathematically, the variance is defined as

$$\text{Var } \theta = \frac{1}{|\Omega|} \int_{\Omega} \theta(\mathbf{x}, t)^2 \, d\Omega, \quad (3)$$

where  $\Omega$  is our computational domain, and  $|\Omega|$  denotes the size (volume or area) of our domain. In the above definition, we have assumed, without loss of generality, a zero mean of the passive scalar field  $\theta$ . Throughout this paper we will be optimizing with respect to this quantity, but we stress again that other norms can be employed without conceptual changes in the optimization procedures.

### 2.3. Complex geometry via penalization

Stirrers will be used to achieve fluid mixing, categorizing our problem as a fluid-structure interaction problem. We will use the the penalization method [10] to approach this problem. Its appeal lies in the simple modification of the governing Navier-Stokes equations by adding external forcing terms. These terms model our solid bodies as Brinkman-style porous media with vanishing permeability  $C_\eta$ . This method has been shown to converge to the exact solid-fluid solution as  $C_\eta$  tends to zero [11]; furthermore, it is able to enforce Dirichlet as well as Neumann boundary conditions on the respective flow variables. The advantage of this method lies in its rather simple implementation, its flexibility in imposing complex boundary conditions, and its numerical efficiency. Moreover, moving solids are straightforwardly treated by remapping masks to a new position, without any need for remeshing or sophisticated grid operations. We will provide a brief overview here; for alternative applications of this method, or a more in-depth coverage of this method, the reader is referred to [27].

In preparation for the fact that we will deal with multiple embedded solids with independent characteristics, we will introduce  $\chi_i$ , a mask function of the  $i$ -th solid by defining

$$\chi_i(\mathbf{x}, t) = \begin{cases} 1, & \text{if } \mathbf{x} \in \Omega_{s,i} \\ 0, & \text{if } \mathbf{x} \in \Omega_f \\ 0, & \text{if } \mathbf{x} \in \Omega_{s,j \neq i} \end{cases} \quad (4)$$

with  $\Omega_{s,i}$  denoting the  $i$ -th solid domain, while  $\Omega_f$  stands for the fluid domain. The global mask  $\chi$  for our computational domain is then given as

$$\chi(\mathbf{x}, t) = \sum_i \chi_i(\mathbf{x}, t). \quad (5)$$

The mask  $\chi$  acts as an indicator function which distinguished between the solid part ( $\chi = 1$ ) and the fluid part ( $\chi = 0$ ) of the computational domain. This indicator function then allows us to

supplement the Navier-Stokes equations (1) by external driving terms that impose a given velocity of the  $i$ -th solid, denoted by  $\mathbf{u}_{s,i}$ , on the fluid and thus model the motion of individual bodies through the fluid.

Assuming Einstein summation over identical indices, we can then state the penalized Navier-Stokes equations as

$$\partial_t \mathbf{u} + \mathbf{u} \cdot \nabla \mathbf{u} + \frac{\chi}{C_\eta} \mathbf{u} - \frac{\chi_i}{C_\eta} \mathbf{u}_{s,i} + \nabla p - Re^{-1} \nabla^2 \mathbf{u} = 0, \quad (6a)$$

$$\nabla \cdot \mathbf{u} = 0, \quad (6b)$$

where  $C_\eta$  is the permeability of the solids (which, for simplicity, we take identical for all solids). It has been shown [28] that an optimal value of  $C_\eta$  is proportional to  $(\Delta x)^2$ , and this leads to accurate numerical results. Recalling the definition of  $\chi_i$ , we note that the equations above reduce to the Navier-Stokes equations (1) in the fluid domain ( $\chi = 0$ ).

Proceeding to the governing equations for the passive scalar  $\theta$ , we also have to apply penalization terms to enforce no-flux boundary conditions at the various solids. The scalar field equation (2) then becomes [29]

$$\partial_t \theta + (1 - \chi) \mathbf{u} \cdot \nabla \theta + \chi_i (\mathbf{u}_{s,i} \cdot \nabla \theta) - \nabla \cdot \left( \left[ Pe^{-1} (1 - \chi) + \frac{\chi}{C_\eta} \right] \nabla \theta \right) = 0. \quad (7)$$

The terms  $(1 - \chi) \mathbf{u} \cdot \nabla \theta$  and  $\nabla \cdot \left( \left[ Pe^{-1} (1 - \chi) + \chi/C_\eta \right] \nabla \theta \right)$  prevent the passive scalar field  $\theta$  advecting or diffusing, respectively, into any of the solids; the term  $\chi_i (\mathbf{u}_{s,i} \cdot \nabla \theta)$  transports the scalar field with the velocity of the  $i$ -th solid.

### 3. Numerical method

The starting point for the discretization of the penalized governing equations is the open-source software `FluSI` [28], a Fourier pseudo-spectral code for fluid-structure interactions. It solves the three-dimensional, incompressible Navier-Stokes equations on equispaced grids using a spectral formulation, adaptive time-stepping and a pressure-projection approach. The inclusion of solid bodies, or complex computational domains, is treated by a Brinkmann-type penalization method; sponge layers are utilized to handle open and outflow boundaries.

Below we give a brief outline of the key features of the numerical methodology and introduce special details that had to be added to suit our goal of mixing enhancement. In particular, we put in place a spatially discrete formulation which will build the basis for an efficient derivation and implementation of an adjoint solver.

#### 3.1. Discretization of the governing equations

Following the discretization strategy of the original `FluSI` code, we replace the continuous spatial derivatives with multiplications of the discretized velocity, pressure and passive scalar fields by a Fourier discretization matrix. We introduce the discrete analog of the continuous derivative according to

$$\frac{\partial}{\partial x_i} \rightarrow \mathbf{A}_i. \quad (8)$$

with  $\mathbf{A}_i$  as an  $n \times n$  matrix where  $n$  is the number of grid points in a single dimension. The associated discrete gradient operator, consisting of  $\mathbf{A}_i$  for the two coordinate directions, is represented by  $\mathbf{A}$ . Furthermore, discretization on an equispaced two-dimensional mesh results in the following variables:  $\mathbf{u}$  represents a  $3 \times n$  vector containing the three velocity components, and  $\chi, \theta$  and  $p$  are  $1 \times n$  vectors representing the mask, passive scalar and pressure field, respectively. In addition, we introduce as  $\mathbf{u}_{s,i}$  the  $3 \times n$  velocity vector of the  $i$ -th solid, as well as the corresponding mask for the same solid, denoted by  $\chi_i$ . We note that  $(\mathbf{u}_{s,i})_j$  is a  $1 \times n$  vector containing the velocity component in the  $j$ -th coordinate direction of the  $i$ -th solid.

With these notations and assuming the Einstein summation convention, we can then state the spatially discretized governing equations in the form

$$\partial_t \mathbf{u} + \mathbf{u}_j \circ [\mathbf{A}_j \mathbf{u}] + \frac{\chi}{C_\eta} \circ \mathbf{u} - \frac{\chi_i}{C_\eta} \circ \mathbf{u}_{s,i} + \mathbf{A}p - Re^{-1} \mathbf{A}_i \mathbf{A}_i \mathbf{u} = 0, \quad (9a)$$

$$\mathbf{A}_i \mathbf{u}_i = 0, \quad (9b)$$

$$\begin{aligned} \partial_t \theta - \mathbf{A}_i \left( [Pe^{-1} (\mathbf{1} - \chi) + \kappa \chi] \circ \mathbf{A}_i \theta \right) + (\mathbf{1} - \chi) \circ \mathbf{u}_j \circ [\mathbf{A}_j \theta] \\ + \chi_i \circ (\mathbf{u}_{s,i})_j \circ [\mathbf{A}_j \theta] = 0 \end{aligned} \quad (9c)$$

where we used the Hadamard (element-wise) product  $\circ$  (see [30]). We invoke an operator-splitting approach and enforce the continuity equation  $\mathbf{A}_i \mathbf{u}_i = 0$  via a pressure Poisson equation which reads

$$\mathbf{A}_j \mathbf{A}_j p + \mathbf{A}_i (\mathbf{u}_j \circ [\mathbf{A}_j \mathbf{u}_i]) + \mathbf{A}_i \left[ \frac{\chi}{C_\eta} \circ \mathbf{u} - \frac{\chi_i}{C_\eta} \circ \mathbf{u}_{s,i} \right] = 0. \quad (10)$$

We will consider the masks  $\chi_i$  (representing the shape of the solid objects) and the velocities  $\mathbf{u}_{s,i}$  (representing their speed) as the control variables of the governing set of equations which need to be adjusted to influence and optimize mixing efficiency. The velocities  $\mathbf{u}_{s,i}$  can further be specified in the form

$$\mathbf{u}_{s,i} = \mathbf{u}_{C_i}(t) + \omega_i(t) \mathbf{r}_i(\mathbf{x}), \quad (11)$$

where  $\mathbf{u}_{C_i}(t)$  is the time-dependent velocity of the center of the solid,  $\omega_i(t)$  is the rotational speed of the solid about its center, and  $\mathbf{r}_i$  denotes the distance from the same center.

The above spectrally discretized governing equations are nonlinear, and special care has to be exercised to avoid numerical instabilities due to aliasing errors stemming from the quadratic nonlinearities. In the original approach (FluSI), aliasing errors have been eliminated by using the  $\frac{2}{3}$ -rule: higher-resolution spectral transforms in combination with zero-padding and downsampling are used to circumvent contamination of the lower wavenumbers by mapped higher ones. In our implementation, a spectral cut-off filter (suggested in [31]) has been used instead, as it has been found more efficient for our problem.

### 3.2. Numerical implementation of masks

The representation of solid bodies on an underlying Cartesian grid calls for a transfer of geometric information onto the background mesh. This transfer is accomplished by a mollified delta-function, smoothing the otherwise discontinuous mask onto the grid and thus avoiding numerical

inaccuracies and instabilities [32]. We choose the widely used, piece-wise defined function

$$\chi_i(\mathbf{x}, t) = \begin{cases} 1, & \text{for } |f| < r_i \\ \frac{1}{2} \left( 1 + \cos \left( \frac{\pi(f - r_i)}{2h} \right) \right) & \text{for } r_i < |f| < r_i + 2h \\ 0, & \text{otherwise} \end{cases} \quad (12)$$

where  $f$  is some parametric form for the solids we wish to study. We note that  $h$  is proportional to the grid size,  $\Delta x$ , and as  $\Delta x \rightarrow 0$  the function  $\chi_i$  tends to a Heaviside function [28].

#### 4. Optimization using adjoint methodology

The effectiveness of mixing in binary fluids can be quantified by a variety of measures. In this article, we concentrate on the variance of the passive scalar defined in section 2.2, while being fully aware that fractional Sobolev norms of the same quantity, as used, e.g., in [33], are mathematically more suited for mixing problems. The choice of norm, however, does not markedly alter the computational framework introduced below. The choice of the variance is thus for convenience and for the sake of a less cluttered notation. With this choice, we determine the quantity we seek to minimize as

$$\mathcal{J} = \frac{1}{V_\Omega} \int_\Omega \theta^2 \, d\Omega \Big|_{T^F} \quad (13)$$

which constitutes the cost functional  $\mathcal{J}$  for our optimization. In the above expression,  $T^F$  denotes the final time. We note that this particular choice of  $\mathcal{J}$  would lead to unconstrained optimization, as there is no bound on the energy we are able to inject into the system. Therefore, we modify our cost functional with the addition of a term that constrains the energy we supply for the optimal strategy. This enhanced cost functional then takes the form

$$\mathcal{J} = \frac{1}{V_\Omega} \int_\Omega \theta^2 \, d\Omega \Big|_{T^F} + \lambda \int_0^{T^F} \sum_i [(\mathbf{u}_{s,i})_j \chi_i]^H R_i [(\mathbf{u}_{s,i})_j \chi_i] \, dt \quad (14)$$

where we choose  $R_i$  such that the energy penalization constitutes a valid norm. In line with the semi-discretized formulation above, we express the discretized cost functional in the form

$$\mathcal{J} = \frac{\theta^H \mathbf{M} \theta}{V_\Omega} \Big|_{T^F} + \lambda \int_0^{T^F} \sum_i [(\mathbf{u}_{s,i})_j \chi_i]^H \mathbf{R}_i [(\mathbf{u}_{s,i})_j \chi_i] \, dt \quad (15)$$

where  $\mathbf{M}$  is a symmetric, positive definite weight matrix, taking into account the grid resolution and (possible) spatial weightings,  $\mathbf{R}_i$  denotes a positive definite diagonal matrix and the  $^H$  refers to the conjugate transpose of the relevant matrix/vector. We note that for real quantities this simply reduces to the transpose. The user-specified parameter  $\lambda$  controls the weight of the penalization term. With no spatial preference and our uniform spatial mesh of  $n^2$  grid points, the weight matrix  $\mathbf{M}$  is simply a diagonal matrix of the form

$$\mathbf{M} = \left( \frac{1}{n} \right)^2 \mathbf{I} \quad (16)$$

with  $\mathbf{I}$  as the identity matrix.

At this point, we will briefly elaborate on the control parameters we use to minimize the variance. The framework is sufficiently flexible to manipulate various internal or external parameters, but we will concentrate – in view of possible industrial applications – on time-independent variables, specifically the shape  $\chi_i$  of (multiple) stirrers and their rotational speed  $\omega_i$ . These quantities can be altered between iterations using the optimality conditions, but during the forward solution they remain constant in time.

A final observation is the fact that our energy penalization is not a proactive measure, but is instead reactive. When a new optimized solution is applied, the energy penalization refers to the energy of the unoptimized system. Therefore, a situation could arise where the optimization step ventures beyond physical constraints and introduces singularities that prevent the energy penalization from properly taking effect. For this reason, it is imperative to achieve a proper balance between imposing too stringent an energy penalization and thus stifling the system, and too weak a penalization, yielding potentially unphysical scenarios.

#### 4.1. Introducing Lagrange multipliers or adjoint variables

We note that the cost functional  $\mathcal{J}$  is a function of  $\theta$ , which is implicitly influenced by  $\mathbf{u}$ ,  $\mathbf{u}_s$  and  $\chi$ . To be able to optimize our control variables, we need to embed these in an augmented cost functional  $\mathcal{L}$  which explicitly expresses these various dependencies. This is achieved by including the governing equations as well as  $\mathcal{J}$  in a single functional, given by

$$\begin{aligned}
\mathcal{L} = \mathcal{J} - \int_0^{T^F} & (\mathbf{u}^\dagger)_k^H \mathbf{M} \left\{ \partial_t \mathbf{u} + \mathbf{u}_j \circ [\mathbf{A}_j \mathbf{u}] + \frac{\chi}{C_\eta} \circ \mathbf{u} - \frac{\chi_i}{C_\eta} \circ \mathbf{u}_{s,i} + \mathbf{A}p - Re^{-1}[\mathbf{A}_i \mathbf{A}_i \mathbf{u}] \right\}_k \\
& + p^\dagger, H \mathbf{M} \left\{ [\mathbf{A}_i \mathbf{A}_i] p + \mathbf{A}_i (\mathbf{u}_j \circ [\mathbf{A}_j \mathbf{u}_i]) + \mathbf{A}_i \left[ \frac{\chi}{C_\eta} \circ \mathbf{u} - \frac{\chi_i}{C_\eta} \circ \mathbf{u}_{s,i} \right] \right\} \\
& + \theta^\dagger, H \mathbf{M} \left\{ \partial_t \theta + (\mathbf{1} - \chi) \circ \mathbf{u}_j \circ [\mathbf{A}_j \theta] - \chi_i \circ (\mathbf{u}_{s,i})_j \circ [\mathbf{A}_j \theta] \right. \\
& \left. - \mathbf{A}_i ([Pe^{-1}(\mathbf{1} - \chi) + \kappa \chi] \circ \mathbf{A}_i \theta) \right\} + \chi_i^\dagger, H \mathbf{M} [\chi_i - g_i(\mathbf{x}, t)] dt \\
& - \omega_i^\dagger, H \mathbf{M} [\omega_i - z_i]. \tag{17}
\end{aligned}$$

Here, we have introduced Lagrange multipliers or adjoint variables, denoted by the superscript  $\dagger$ . The adjoint variables enforce the constraints given by the governing equations, i.e.,  $\mathbf{u}^\dagger$  enforces the time evolution of  $\mathbf{u}$ ,  $p^\dagger$  the pressure Poisson equation, and  $\theta^\dagger$  is associated with the equation governing the passive scalar field. Lastly,  $\chi^\dagger$  and  $\omega^\dagger$  ensure that the conditions which define the embedded solids are satisfied. We use this semi-discretized framework, rather than a continuous approach that requires the explicit enforcement of boundary conditions, for reasons of greater simplicity, flexibility and functionality when it comes to optimizing mixing by manipulating  $\chi$  and  $\mathbf{u}_s$ . The entire information related to the solids is encapsulated in the penalization terms, and is thus easily captured by associated Dirichlet, Neumann or Robin boundary conditions – without the need to include supplementary terms in the augmented Lagrangian  $\mathcal{L}$ . Moreover, in the ensuing derivation of the adjoint equations, the appropriate boundary conditions on the solids will be fully encoded in the discretized penalization terms, making the resulting numerical implementation substantially simpler and less error-prone.



The key to deriving the optimality conditions is to minimize the augmented cost functional  $\mathcal{L}$  by taking first variations of  $\mathcal{L}$ , i.e., enforcing  $\delta\mathcal{L} = 0$ . Since  $\delta\mathcal{L}$  depends on several independent variables, including the adjoint variables, we require that each individual variation is in effect zero. Proceeding along this line, we note that the first variation with respect to the adjoint variables recovers the original governing equations. We then continue by focusing on the variation with respect to the direct variables which will ultimately produce a governing equation for the adjoint variables. For the sake of clarity, some explicit parts of this calculation have been relegated to the appendix. The full adjoint equations defining  $u^\dagger$ ,  $p^\dagger$  and  $\theta^\dagger$  are as follows:

$$\begin{aligned} \partial_t \mathbf{u}_i^\dagger - \Pi_k^\dagger \circ [\mathbf{A}_i \mathbf{u}_k] - \mathbf{A}_j^H [\mathbf{u}_j \circ \Pi_i^\dagger] - \frac{\chi}{C_\eta} \circ \Pi_i^\dagger + Re^{-1} \mathbf{A}_j^H \mathbf{A}_j^H \mathbf{u}_i^\dagger \\ - (\mathbf{1} - \chi) \circ \theta^\dagger \circ [\mathbf{A}_i \theta] = 0 \end{aligned} \quad (18a)$$

$$\mathbf{A}_j^H \Pi_j^\dagger = 0 \quad (18b)$$

$$\begin{aligned} \partial_t \theta^\dagger - \mathbf{A}_j^H [(\mathbf{1} - \chi) \circ \mathbf{u}_j \circ \theta^\dagger] + \mathbf{A}_i^H [(Pe^{-1}(\mathbf{1} - \chi) + \kappa\chi) \circ \mathbf{A}_i^H \theta^\dagger] \\ - \mathbf{A}_j^H [\chi_i \circ (\mathbf{u}_{s,i})_j \circ \theta^\dagger] = 0 \end{aligned} \quad (18c)$$

with initial conditions

$$\mathbf{u}^\dagger(\mathbf{x}, T^F) = 0, \quad \theta^\dagger(\mathbf{x}, T^F) = \frac{2\theta}{\Omega}. \quad (19)$$

The optimality conditions, stemming from the first variation with respect to the control variables, are found to be

$$\begin{aligned} \chi_i^\dagger &= [(2\lambda R_i)((\mathbf{u}_{s,i})_j \circ \chi_i)] \circ (\mathbf{u}_{s,i})_j \\ &+ \left[ \theta^\dagger \circ [\mathbf{A}_j \theta] - \frac{\Pi_j^\dagger}{C_\eta} \right] \circ (\mathbf{u}_j - (\mathbf{u}_{s,i})_j) + (\kappa - Pe^{-1}) \mathbf{A}_j^H \theta^\dagger \circ \mathbf{A}_j \theta \end{aligned} \quad (20a)$$

$$\omega_i^\dagger = \int_0^{T^F} (\chi_i \circ \mathbf{h}_j(\phi))^H \left( (2\lambda R_i)((\mathbf{u}_{s,i})_j \circ \chi_i) + \frac{\Pi_j^\dagger}{C_\eta} - \theta^\dagger \circ [\mathbf{A}_j \theta] \right) dt \quad (20b)$$

where  $\Pi_i^\dagger = \mathbf{u}_i^\dagger + \mathbf{A}_i^H p^\dagger$ .

We note that since rotation is more conveniently defined in polar coordinates (yet we work in Cartesian coordinates), we introduce the vector-valued function  $\mathbf{h}$ , which transforms the radial velocity from one coordinate system to the other as follows

$$\mathbf{h}_1(\phi) = -\sqrt{(\mathbf{x}^2 - \mathbf{x}_0^2)} \sin \phi, \quad (21a)$$

$$\mathbf{h}_2(\phi) = \sqrt{(\mathbf{x}^2 - \mathbf{x}_0^2)} \cos \phi, \quad (21b)$$

where  $\phi$  is the angle of the point  $\mathbf{x}$  with respect to the horizontal axis.

When considering the above system of equations, we note that we have to simultaneously solve the direct and adjoint equations, as well as the optimality condition. Rather than following this procedure, it is customary to solve the direct and adjoint equations exactly, and to iterate on the

optimality condition, until a user-specified criterion is satisfied. With this approach, we use the gradient with respect to the control variables to advance the solution towards an optimum. We recall that our system is nonlinear, which necessarily implies that we may not achieve convergence to a global optimum; instead, only a local optimum may be guaranteed.

#### 4.2. Summary of algorithm

The system of equations, reformulated as an iterative scheme, coupled with an optimization strategy, completes the full algorithm for computing optimal mixing strategies.

The step-by-step procedure advances along the following lines. Starting with an initial (guessed) mixing strategy, we solve the direct (forward) problem over a chosen time horizon from  $t = 0$  to  $t = T^F$ . In a second step, we turn to the adjoint equations, which advance the adjoint variables backwards in time, from  $t = T^F$  to  $t = 0$ . During this step, it is important to notice that, owing to the nonlinearity of the direct problem, there is an explicit dependence of the adjoint equations on the direct variables. For this reason, we have to store the direct variables during the forward sweep and inject them, at the appropriate time steps, into the adjoint equations. For high-resolution cases and large time horizons, we cannot afford to store all necessary direct variables. In this case, we refer to checkpointing, where we store relevant direct information at specific checkpoints in time. From these checkpoints, we then reconstruct the necessary solutions as they are needed in the adjoint equations. In this manner, we trade memory limitations for a (minor) decline in run-time efficiency.

The algorithmic steps of the full optimization scheme are then:

1. We begin by running our forward solution from  $t = 0$  to  $t = T^F$ , solving our discretized and penalized governing equations (9) and (10). At this point we have specifically chosen checkpoints, at which we save our state variables to disk. We aim to have sufficient checkpoints such that (i) the memory required to save all state variables to RAM does not exceed our resources, and (ii) efficiency of reading and writing to disk is ensured.
2. Once we have reached the endpoint of our simulation at  $t = T^F$ , we run our program forward from our last checkpoint, say  $t_n$ , starting from the state that was saved at this point, to  $T^F$ . During this forward solution, we now ensure that we save the required state variables in RAM for each time step.
3. When we reach  $T^F$ , we begin to run the adjoint simulation backwards in time from  $T^F$  to  $t_n$ . We have all the relevant forward variables in RAM, and so can feed them into the adjoint equations (18) at the correct time step.
4. Once we arrive at  $t_n$  with the adjoint simulation, we save the last state of the adjoint to RAM, making sure we have continuity in the adjoint variables across checkpoints. We then clear the memory and begin with running the forward problem from  $t_{n-1}$  to  $t_n$ , once again saving flow fields to RAM.
5. We repeat steps 2-4, moving successively backwards in the checkpoints until we reach the initial starting time  $t_0 = 0$ . At this point, we evaluate the final time conditions for the quantities we wish to optimize and supply these to our optimization routine to generate the new (and improved) mixing strategy for our system.
6. The direct-adjoint looping strategy is continued until a user-specified criterion is reached; at this time, the simulations terminate.

### 4.3. Examples of mixing optimization

We will induce mixing in our geometries by embedding moving stirrers of elliptical cross-section. These stirrers will move on a pre-determined path. The entire configuration is contained in a circular vessel. Even though our formalism allows for a point-by-point definition and manipulation of the stirrer geometry, we will instead use the parametric form introduced in equation (12) with  $f$  taking the form

$$f = \left[ \left( \frac{(x - x_{0,i}) \cos \alpha_i - (y - y_{0,i}) \sin \alpha_i}{a_i} \right)^2 + \left( \frac{(x - x_{0,i}) \sin \alpha_i + (y - y_{0,i}) \cos \alpha_i}{b_i} \right)^2 \right]^{\frac{1}{2}}, \quad (22)$$

where  $x_{0,i}$  and  $y_{0,i}$  denote the center of the elliptical solid  $i$ ,  $a_i$  and  $b_i$  are the two perpendicular axes, respectively, and  $\alpha_i$  is the angle of attack with respect to the horizontal coordinate direction. This parameterization will yield a more low-dimensional version of general shape optimization. It is possible to optimize the axes  $a_i$  and  $b_i$  independently, however, as we seek to enforce a constant cross-sectional area of our stirrers, we will enforce  $a_i b_i = 1$ .

#### 4.3.1. Shape optimization

The above simplifications for the optimization of the stirrer shape carries through to the optimality condition that furnishes, together with the optimization routine, a new and improved geometry after every iteration. With the area constraint in place, we only control the axis  $a_i$  and reformulate the cost functional gradient with respect to our (restricted) control variables, expressed in terms of the adjoint variable  $a_i^\dagger$ , as follows:

$$\begin{aligned} a_i^\dagger &= \int_0^{T^F} \frac{\partial \mathcal{L}}{\partial a_i} dt, \\ &= \int_0^{T^F} \frac{\partial \mathcal{L}}{\partial \chi_i} \frac{\partial \chi_i}{\partial f} \frac{\partial f}{\partial a_i} dt. \end{aligned} \quad (23)$$

In the above expression, the gradient  $\frac{\partial \mathcal{L}}{\partial \chi_i}$  follows directly from equation (17). From equation (12) we can see that

$$\frac{\partial \chi_i}{\partial f} = \begin{cases} 0, & |f(x, y, a_i, b_i)| < r_i, \\ -\frac{\pi}{4h} \sin\left(\frac{\pi(f - r_i)}{2h}\right), & r_i < |f(x, y, a_i, b_i)| < r_i + 2h, \\ 0, & \text{otherwise.} \end{cases} \quad (24)$$

The remaining derivative  $\frac{\partial f}{\partial a_i}$  is straightforward. The above expressions can then be combined to obtain  $a_i^\dagger$ , which is then used to optimize the axis for optimal mixing.

### 4.3.2. Speed optimization

One may note that our definition of the solid velocity, equation (11), includes a rotational term, linked to  $\omega_i$ , as well as the general velocity term  $\mathbf{u}_{C_i}$ . It is certainly possible to optimize both terms independently; but this will be left as a future effort. As this article focuses primarily on the algorithm and its validation, we choose to draw our attention on the optimization of the rotational velocity  $\omega_i$ , as a representative test of the direct-adjoint optimization framework.

## 5. Validation of gradient direction and optimization results

### 5.1. A simple gradient check

Before embarking on various test cases for the optimization of mixing strategies, we perform a consistency check of our adjoint framework. To this end, we consider a scalar control variable  $q$  together with its adjoint equivalent  $q^\dagger$ . The optimality condition

$$\frac{\delta \mathcal{L}}{\delta q} = 0 \quad (25)$$

then establishes a link between the adjoint control variable  $q^\dagger$  and the cost functional gradient  $\delta \mathcal{J} / \delta q$ . We have

$$q^\dagger = -\frac{\delta \mathcal{J}}{\delta q} \quad (26)$$

which we will use to test our direct-adjoint system. More specifically, we evaluate the right-hand side by a finite-difference approximation according to

$$\frac{\delta \mathcal{J}}{\delta q} \approx \frac{\mathcal{J}(q + \epsilon) - \mathcal{J}(q)}{\epsilon}, \quad (27)$$

for a small value of  $\epsilon$ . This expression is based on the forward problem only. This expression is then contrasted to the value  $q^\dagger$  which stems from the adjoint system. While we will not be able to make a quantitative comparison between the two expressions, we can match the sign-distributions of the various gradients. In other words, we evaluate the consistency relation

$$\text{sgn}(q^\dagger \cdot \epsilon) = \text{sgn}(\mathcal{J}(q) - \mathcal{J}(q + \epsilon)). \quad (28)$$

The results of this check is listed in table (1), where we show that the sign combinations across all scenarios (using the axis  $a$  and the rotational speed  $\omega$  as control variables in our case) match accordingly. This test verifies the correct directionality of the adjoint-based gradient which, in turn, will ensure an improved mixing strategy from iteration to iteration.

### 5.2. Definition of test configurations

To further validate the direct-adjoint optimization framework for enhancing mixing, we choose a suite of test problems that progressively challenge the computational procedure but still comply with our intuition for an optimal solution. The purpose of this exercise is less in treating a physically

	$a + \epsilon$	$a - \epsilon$
$\omega + \epsilon$	+	+
$\omega - \epsilon$	-	-

	$\epsilon a^\dagger$	$-\epsilon a^\dagger$
$\epsilon \omega^\dagger$	+	+
$-\epsilon \omega^\dagger$	-	-

Table 1: Consistency check based on the sign distribution of the control variable gradient: (left) based on a finite-difference approximation of the forward problem, (right) based on the adjoint system.

interesting case, but rather in demonstrating the efficiency and effectiveness of the adjoint-based optimization scheme.

In each chosen scenario all involved stirrers begin as circular cylinders with unit radius and an initial rotational speed of 0.25 (either in the clockwise or anti-clockwise direction). The various configurations, ranging from a stationary, rotating cylinder to five rotating cylinders, to a moving and rotating cylinder, are sketched in figure 1. For all simulations, we chose a Reynolds number of  $Re = 1000$  and a Péclet number of  $Pe = 1000$ . The time horizon for the optimization is  $T^F = 32$ ; and the penalization term  $C_\eta$  has been set to  $C_\eta = 0.001$ , where the value was chosen in accordance with similar scenarios as present in FLuSI as well as being consistent with the value reliant on the grid distance. The passive scalar  $\theta$  is initially stratified with  $\theta = 1$  in the upper half of the cylindrical domain  $\Omega$  and  $\theta = 0$  in the lower half. In all cases, we will present the results for a weakly and highly penalized optimization setting (choosing the parameter  $\lambda$ ).

### 5.3. Case 1: one stationary, rotating stirrer

We commence by considering the case of a single, rotating (initially cylindrical) stirrer located in the center of a circular vessel. We optimize the rotational speed as well as the stirrer shape which we assume generally elliptical. By lengthening or shortening the the stirrer’s axis and increasing the speed at which the stirrer spins, we seek to enhance the mixing efficiency (measured by the variance of the passive scalar) over a given time interval. We place limitations on the shape of the stirrer by holding constant its cross-sectional area and on the speed of the rotation by capping the maximum energy injected into the mixture. We note that the shape of the stirrer directly affects the energy transferred into the fluid, as highly eccentric shapes require a larger input effort, but simultaneous may yield improved mixing.

This case serves as a first benchmark for the direct-adjoint optimization framework; in particular, we wish to gauge the convergence behavior, probe the influence of the penalization parameter, and assess the physical fidelity of the obtained solution.

#### 5.3.1. Highly penalized system

As a proof of concept, we present the results of our optimizations with a rather high penalization parameter of  $\lambda_1 = 10^{-3}$ . As expected, the optimization increases the rotational velocity and the eccentricity of the stirrer. The progression in these control parameters versus the number of iterations is shown in figure 2a where we observe a monotone shift towards more eccentric shapes (in red) and a gradual increase in the rotation speed  $\omega$  (in blue). After six iterations, convergence is achieved, caused by the input energy penalization.

Considering the evolution of the variance over the chosen time interval  $t \in [0, T^F]$  we observe a clustering of the various iterations; it appears that an over-penalization has allowed only marginal improvement in mixing efficiency. This matches the convergence of the shape and rotational speed variables in figure 2a.

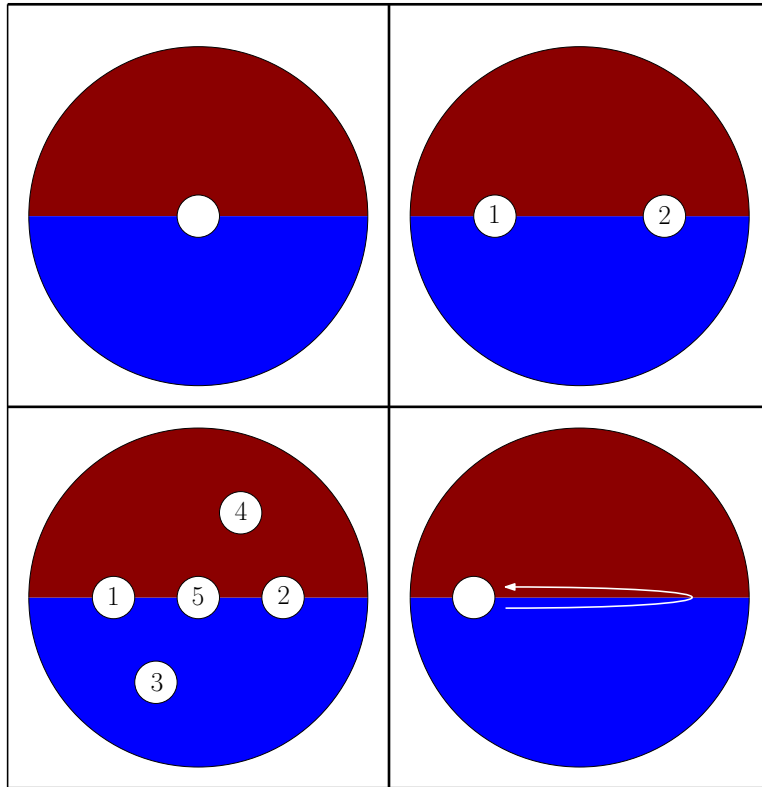


Figure 1: Sketch of the initial configurations for the four test cases. (top left) Case 1: one centered cylinder rotating about its axis. (top right) Case 2: two cylinders on the horizontal axis, rotating in opposite directions. (bottom left) Case 3: five rotating cylinders, placed such that three cylinders are aligned along the horizontal axis, while the remaining two are vertically offset. (bottom right) Case 4: one rotating cylinder moving from left to right with the velocity of the horizontal movement dictated by a cos-function.

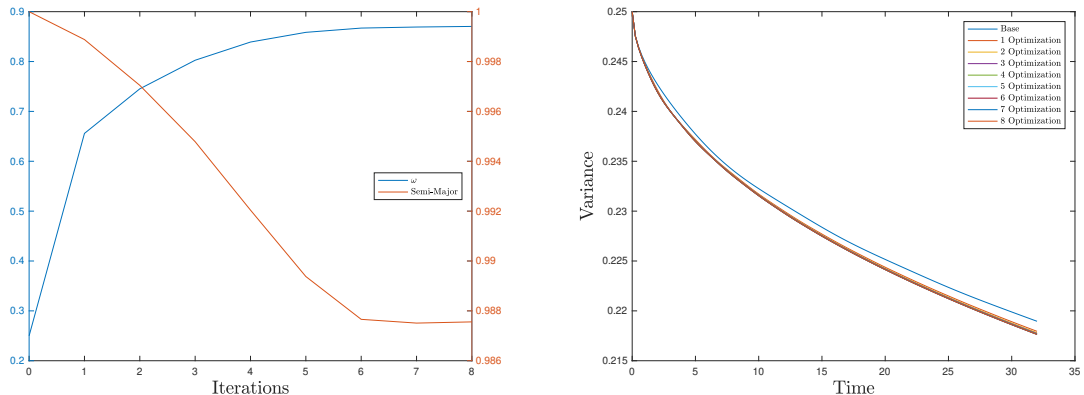


Figure 2: Case 1: mixing optimization using one stationary, rotating stirrer. A highly penalized optimization setting has been used. (a) Rotational speed  $\omega$  and axis  $a$  versus the number of direct-adjoint iterations. (b) Variance of the passive scalar versus time  $t \in [0, T^F]$ .

From a physical point of view, the marginal mixing improvement can be attributed to the inability of the (penalized) stirrer to produce small-scale structures which could be dissipated or to induce significant advective mixing processes. Instead, after nine iterations we remain within the solid-body rotation regime, an example of which is shown in the left column of figure 4. The lack of small-scale structures renders diffusion ineffective, and explains the disappointing decrease in variance; the final mixing is solely due to the diffusion of an extended fluid interface created by the faster spinning (near-)cylinder.

### 5.3.2. Weakly penalized system

To induce more effective mixing, the system must be able to use advective processes to create small-scale structures and filaments which then give rise to significant mixing by diffusion. The highly penalized system of the previous section does not venture into the proper parameter regime to encourage this behavior. For this reason, we drastically lower the penalization value to  $\lambda = 10^{-4}$ .

When considering the variances that follow from each direct-adjoint iteration in figure 3a, we note a clustering over the first optimizations, similar to the highly penalized approach. In this range, we still remain in the solid-body regime and thus solely rely on diffusion for our mixing. However, we note that the seventh and eighth iteration brings about a marked change and leads to a significant decrease in the variance when compared to the preceding steps (see figure 3b for a closer view). The associated stronger mixing is created by the availability of an advective process caused by the elliptic stirrer that is now sufficiently elongated (and spinning sufficiently fast) to shed vortices off its tips. These vortices form the sought-after small-scale structures that intensify the diffusion process by increasing the length of the interface between the two fluids. These increased small scale dynamics enhance the adjoint's ability to create further mixing significantly and therefore result in the drastic decrease in variance as can be observed in figure 3a.

During the optimization, we notice a substantial increase in the adjoint variables – to a degree that requires the marked reduction of the step-size in the optimization routine. This increase is expected, as a more efficient process that accomplished mixing is available after the stirrer has been modified to induce vortex shedding. In other words, after six iterations on the cost functional

surface, we have reached the edge of the diffusion-dominated plateau and progressed towards lower variances by exploiting advection-diffusion-dominated mixing. The high penalization parameter  $\lambda$  in the previous section inhibited the exploration of this regime.

The shape of the variance for the ninth iteration (see figure 3a) exhibits a leveling off during the later stages of the direct simulation (between  $t \approx 25$  and  $t = 32$ ). This suggests that at this point the mixing process driven by the elliptical stirrer is nearly complete, and any further mixing is primarily due to diffusion. In fact, when comparing the gradient of the variance to previous iterations, we observe a corresponding similarity and thus can conclude that advection no longer plays an important role. This conclusion is further corroborated by regarding the right-hand column of figure 4, which shows snapshots from the final iteration; the uniformity of the passive scalar field  $\theta$  is evident towards the end of the temporal optimization horizon.

While this simple example has supplied information about the convergence behavior and the role of the penalization parameter in including or excluding physical mixing strategies to accomplish optimal mixing results, we now proceed to more complex cases and further probe the direct-adjoint optimization framework.



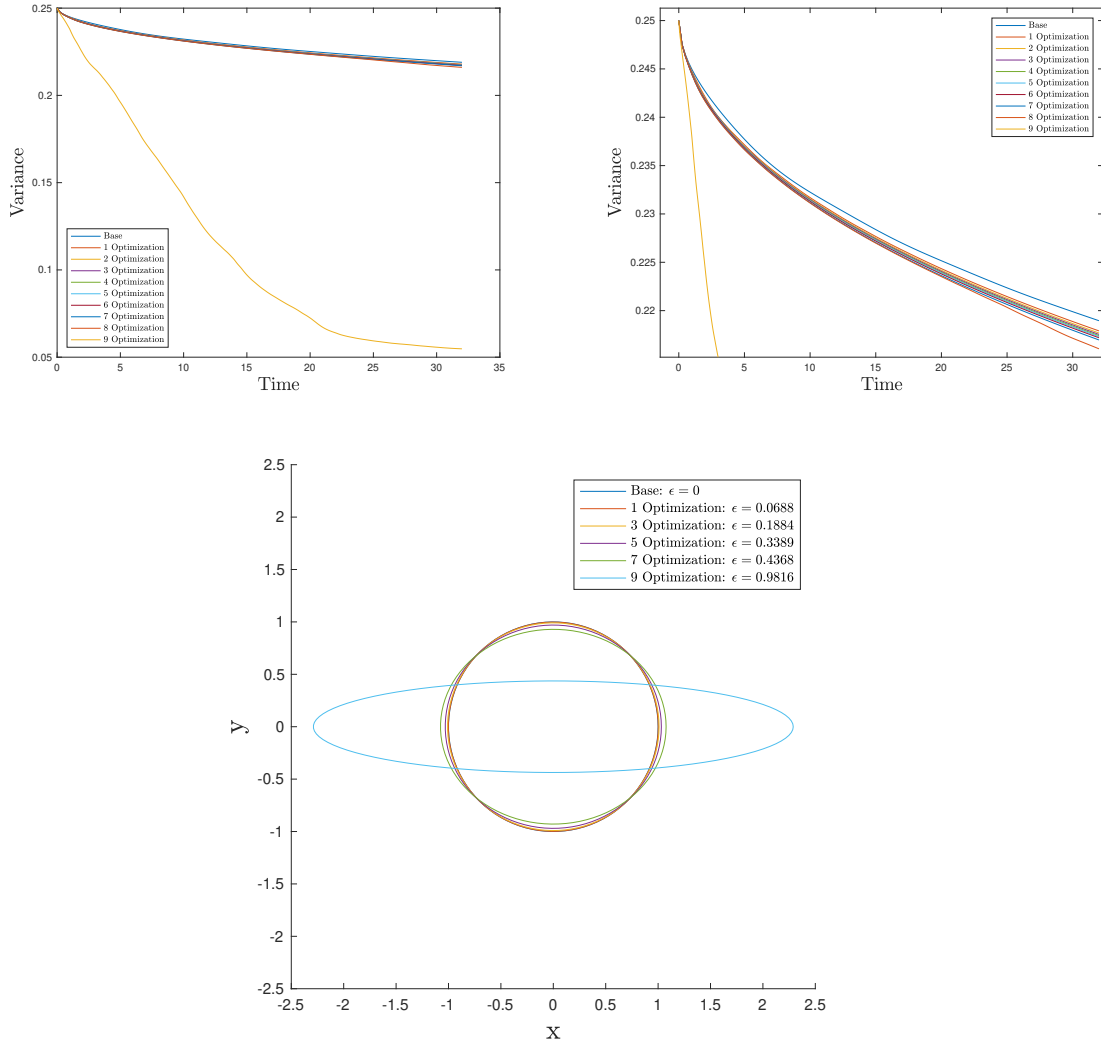


Figure 3: Case 1: mixing optimization using one stationary, rotating stirrer. (a) Variance, as defined in equation (3), of the scalar field  $\theta$  versus time  $t \in [0, T^F]$ . (b) Zoomed-in view to illustrate the decrease in variance for the first eight iterations. (c) Contour of cylinder shapes as result of successive iterations.

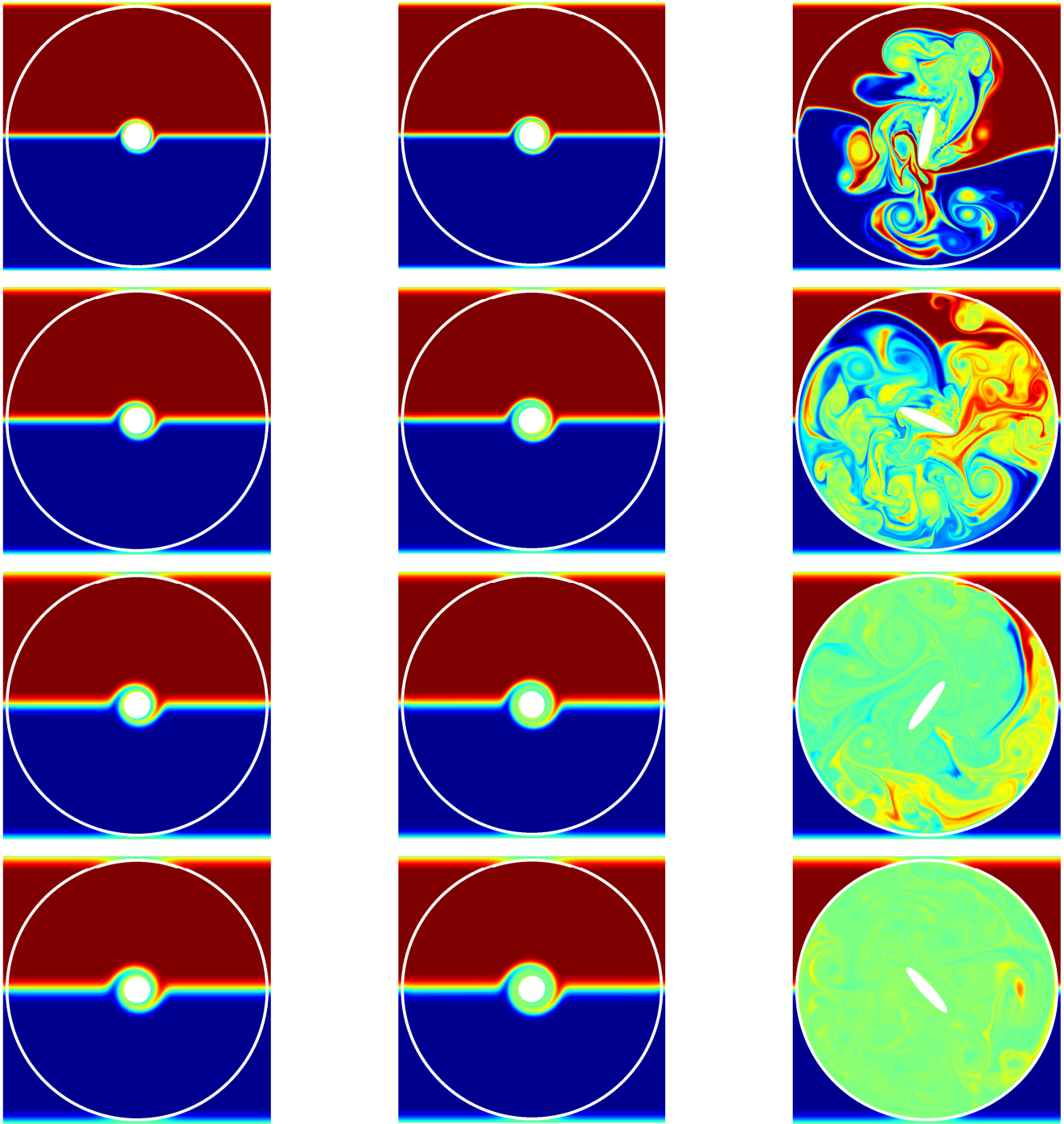


Figure 4: Case 1: mixing optimization using one stationary, rotating stirrer. Left column: unoptimized configuration, with snapshots at  $t = 8, 16, 24, 32$  (top to bottom). Middle Column: after four direct-adjoint optimizations, with snapshots at  $t = 8, 16, 24, 32$  (top to bottom). Right column: after nine direct-adjoint optimizations, with snapshots at  $t = 8, 16, 24, 32$  (top to bottom). For videos of these scenarios please refer to `1Before.mp4`, `1Intermediate.mp4` and `1After.mp4` for the left, middle and right column, respectively.

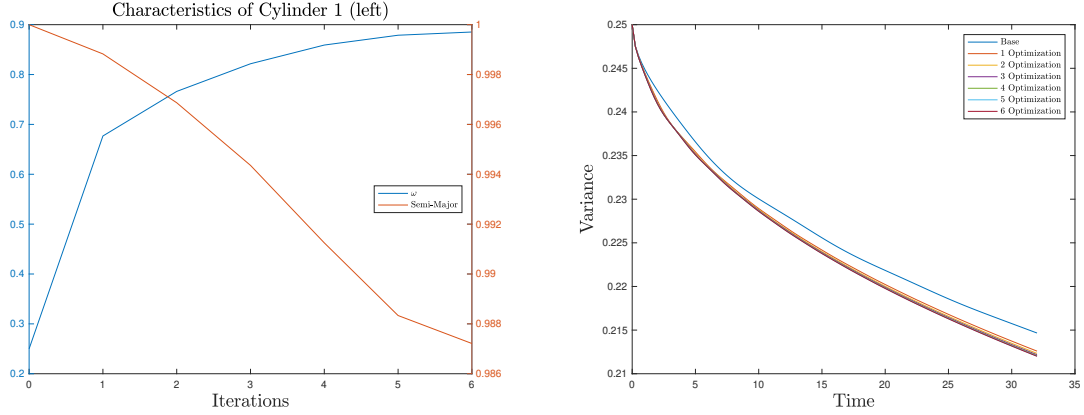


Figure 5: Case 2: mixing optimization using two stationary, rotating stirrers. A highly penalized optimization setting has been used. (a) Rotational speed  $\omega$  and axis length  $a$  versus the number of direct-adjoint iterations for the first (left) cylinder. (b) Variance of the passive scalar versus time  $t \in [0, T^F]$ .

#### 5.4. Case 2: two stationary, rotating stirrers

We complicate the geometry and optimization scheme by introducing a second stirrer which we place along the horizontal axis of the mixing dish; as before, the initial shape of both stirrers is taken as circular. Again, we also consider the influence of the penalization parameter (controlling the maximum amount of energy added to the system) on the convergence behavior and the chosen physical optimization strategy.

##### 5.4.1. Highly penalized system

We observe, similar to the previous one-cylinder case, that a high energy penalization parameter prevents the optimal mixing strategy to explore options other than solid-body rotation and diffusion of the spinning boundary layer around the (mostly) circular stirrers. With the existence of a second stirrer, there is an additional possibility for the optimization scheme of exiting this regime: by placing the two stirrers close to each other, we can have their respective rotating boundary layers interact and exchange sufficient adjoint (gradient) information to induce advection-dominated strategies and a corresponding drop in variance. In our case, the two stirrers appear unaware of each other; no cooperative strategy is pursued by the optimization scheme and, as a result, little progress is made in improving mixing efficiency.

Figure 5a shows the evolution of the axis length (while maintaining the cross-sectional area) and the rotational speed of the first (left) stirrer as we progress through six iterations of the direct-adjoint looping. We see an increase in the rotational speed, but only an insignificant change in the stirrer's eccentricity. The control variables for the second (right) stirrer are identical to the ones shown in figure 5a. It is not surprising that the temporal evolution of the variance over these six iterations appears rather clustered (see figure 5b).

##### 5.4.2. Weakly penalized system

Applying a lower value of  $\lambda$  to this two-stirrer configuration is expected to yield similar results as observed before: by allowing from energy expenditure, advective processes will become a feasible

option, vortex shedding from elliptical stirrers will commence and substantially more efficient mixing will ensue.

While this behavior is certainly prevalent (as shown in figure 6), when considering snapshots in time after the seventh iteration of the direct-adjoint optimization we observe that while the right stirrer has been optimized into a fast-rotating, elliptical shape (as anticipated), the left cylinder is still nearly circular in nature and appears to only mix by diffusing its rotating boundary layer (see the right column of figure 7). In fact, the bulk of the variance drop can be ascribed to the right stirrer.

This observation highlights an issue and shortcoming of gradient-based optimization. In order for the left stirrer to “engage” in the mixing process, it has to pass through a (locally) less optimal configuration. In other words, we have to first allow an increase in variance contribution from the left stirrer, before we can substantially lower the global variance by having the left stirrer contribute to the overall mixing process. Within our optimization framework, where after every iteration we proceed along the local gradient, this required procedure is excluded. However, this is a well-known and acknowledged issue of gradient-based optimization schemes: we are able to find local minima, but have no guarantee (or strategy) to find a global optimum.

In our case, we can improve the situation by mirroring the control variables of the second (right) stirrer onto the first (left) stirrer. In this manner, we induce sufficient gradients in the cost functional for *both* cylinders to encourage further progress in the reduction of the global variance. In this manner, we achieve lower variance levels than before (see the dashed line in figure 6). The final shape of the stirrers for the improved strategy consists of two ellipses of marked eccentricity, with their respective semi-major axes positioned  $90^\circ$  to each other (the behavior of this improved minimum can be seen in the video `2ImprovedMin.mp4`).

For a more objective manner of reaching a global optimum, sophisticated optimization strategies have to be employed in addition to the gradient-based framework; these strategies require the (commonly stochastic) evaluation of various parameter settings and quickly become prohibitively expensive for large-scale, PDE-based optimizations.

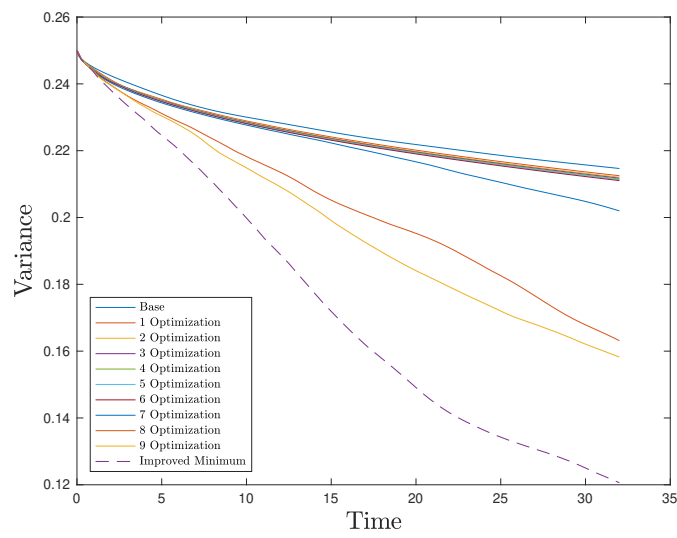


Figure 6: Case 2: mixing optimization using two stationary, rotating stirrers. Variance, as defined in equation (3), of the scalar field  $\theta$  versus time  $t \in [0, T^F]$ . The solid lines represent a local optimum, where the left stirrer remains rather inactive. The dashed line represents an improved optimum, by mirroring the control variables onto the left stirrer before continuing the gradient-based optimization.

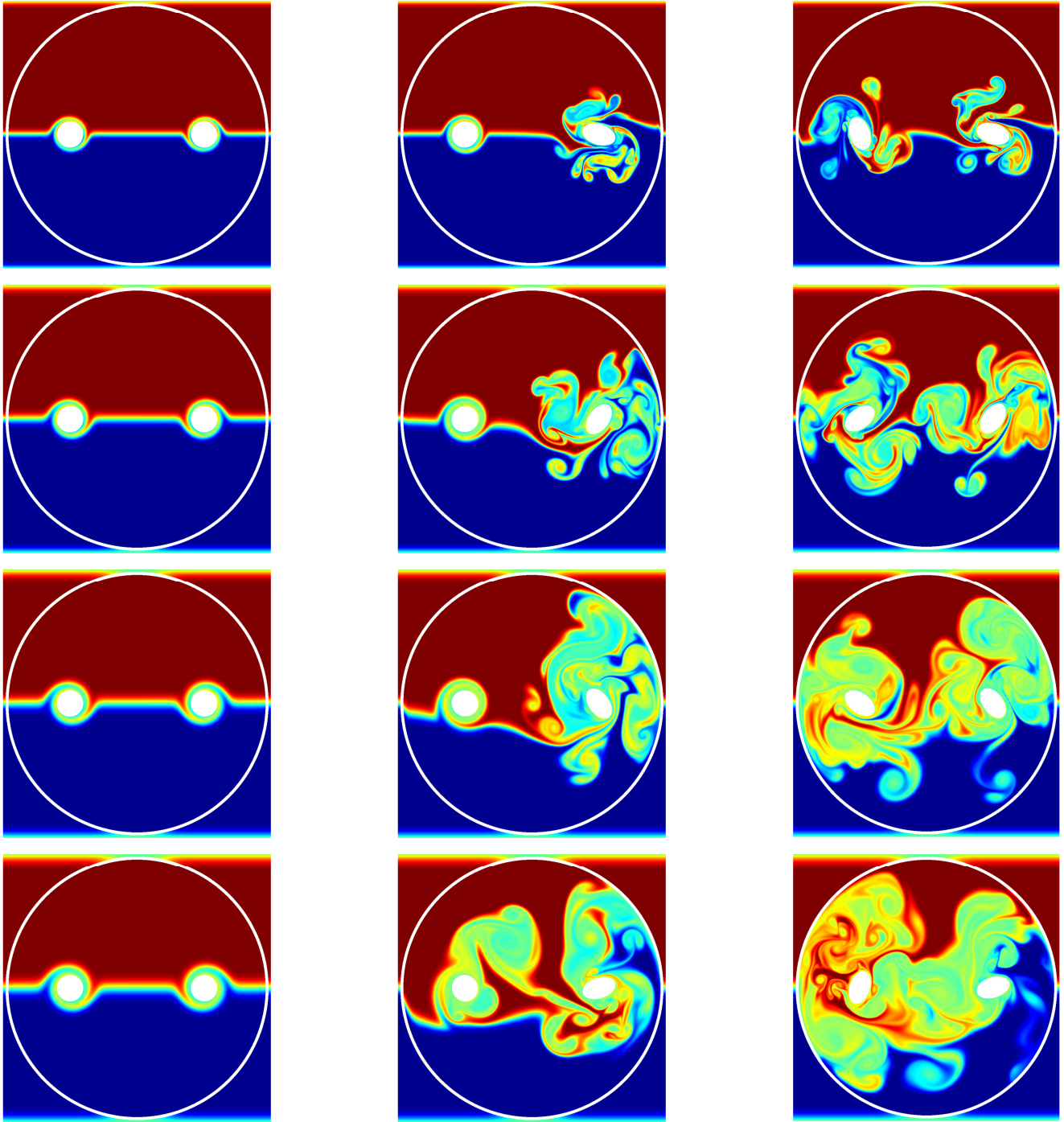


Figure 7: Case 2: mixing optimization using two stationary, rotating stirrers. Left column: unoptimized configuration, with snapshots at  $t = 8, 16, 24, 32$  (top to bottom). Middle column: after seven direct-adjoint optimizations, with snapshots at  $t = 8, 16, 24, 32$  (top to bottom). Right column: Enforced minimum by mirroring the axis length across both cylinders at  $t = 8, 16, 24, 32$ . For videos of these scenarios please refer to `2Before.mp4`, `2After.mp4` and `2ImprovedMin.mp4` for the left, middle and right column, respectively.

### 5.5. Case 3: five stationary, rotating stirrers

Motivated by the previous configuration, we proceed by adding more stirrers and further explore the behavior of the optimization scheme when multiple optima and strategies compete for the best mixing efficiency.

#### 5.5.1. Highly penalized system

To study the behavior of the direct-adjoint optimization scheme on this more complicated geometry, we first impose a high energy penalization, as before. The results are displayed in figure 8, for the stirrers labelled 1,3 and 5 (see 1). While the two stirrers on the horizontal axis show behavior similar to the previous cases (i.e., a tendency towards higher rotational speed and an elliptic shape), eccentricity remains largely unchanged, while the rotational velocity is significantly dampened. At first sight, this may run counter to intuition that suggests that higher speeds result in improved mixing. However, it appears that – under the constraints of a limited energy budget – it is more advantageous to invest input energy into the aligned stirrers rather than squandering it on the offset stirrer that is located in a rather homogeneous tracer field and thus cannot contribute to the global variance drop to any significant degree. For this reason, the optimization scheme (more specifically, the adjoint system) directs focus on the three aligned stirrers that do make a difference.

Regarding the variances of the scalar field in figure 9 we conclude, as before, that we do not fully utilize diffusion *and* advection, which is required for efficient mixing. To exhibit a significant decrease in the variance, we have to explore the weak energy penalization regime.

#### 5.5.2. Weakly penalized system

When removing the constraint of minimal energy expenditure, while still limiting the total amount of energy distributed among the five stirrers, we see the emergence of advection-based mixing. The five stirrers take on elliptical shapes of varying eccentricity and tend to increase in their spin rate. This process induces a complex system of shed vortices that not only introduces small-scale features and thin filaments, but also transports information between the five stirrers. The ensuing optimization scheme then finds an optimal collaborative mixing strategy between the five stirrers that optimizes the global variance while remaining within the imposed energy constraints.

Throughout the initial iterations, no significant information is exchanged between the cylinders, and therefore the off-set cylinders are neglected due to the homogeneity of their surroundings. Even in the low penalization the optimization regards any energy used by these cylinders as wasteful. During subsequent iterations the transport of information is built up but remains negligible. In particular, considering the variances in figure 9, we note that the initial five iterations do not lead to significant improvements in mixedness, as we mainly stay within the previously mentioned solid-body rotation. Once vortex shedding sets in (starting at the sixth iteration, mainly with the central stirrer), however, we see a significantly larger decrease in variance. Continuing further in the optimization, all remaining stirrers are involved in the mixing process, as a jet forms between the central cylinders which interacts with the off-set cylinders implying that energy expended on their rotation will have an effect on the mixing. In particular, the elliptical shape of the stirrers converges towards its final configuration relative to each other.

Similar to the one-cylinder case, our final optimization reaches a point where the predominant mixing process is diffusion and the gradient of the variance is comparable to the purely diffusive limit.

Temporal snapshots of the optimized mixing (after seven iterations) can be observed in figure 10 in the right column. We remark that this is the final optimization, since any further lengthening

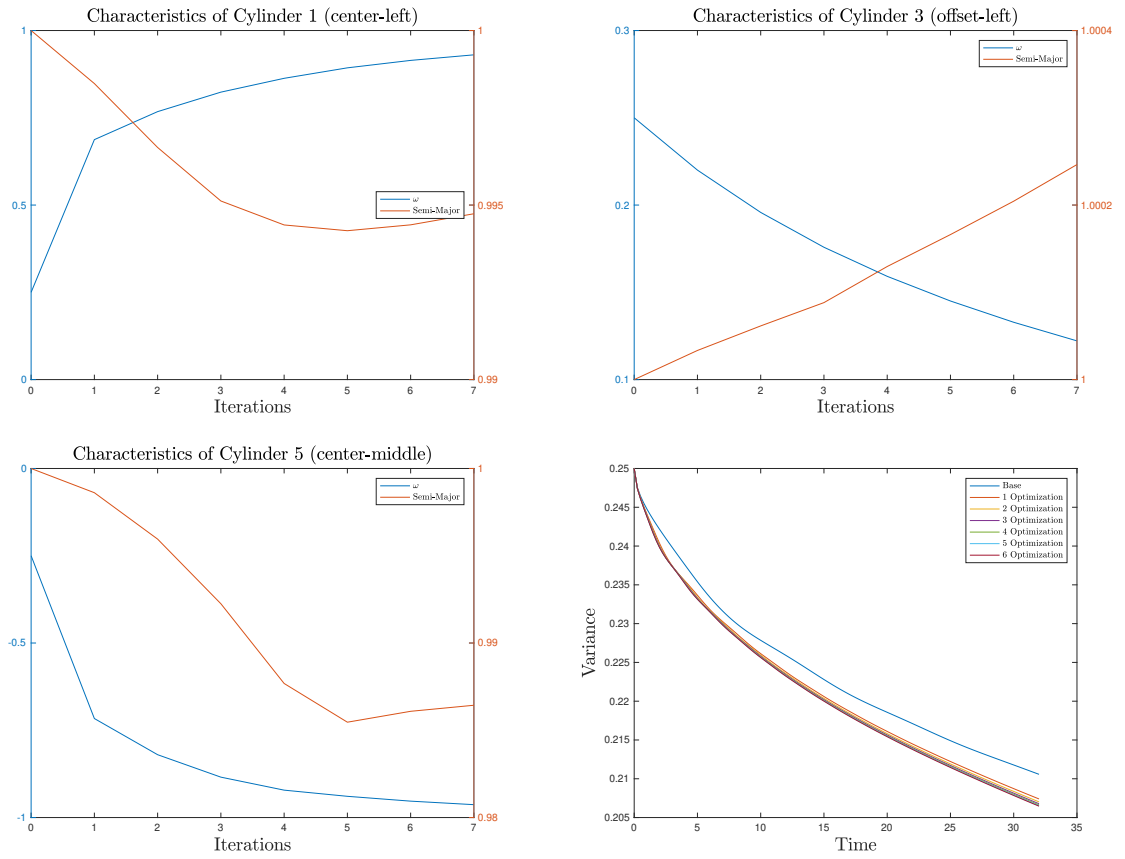


Figure 8: Case 3: mixing optimization using five stationary, rotating stirrers. A highly penalized optimization setting has been used. (a) Rotational speed  $\omega$  and axis  $a$  versus the number of direct-adjoint iterations for the first (left-most) cylinder. (b) Rotational speed  $\omega$  and axis  $a$  versus the number of direct-adjoint iterations for the third (bottom) cylinder. (c) Rotational speed  $\omega$  and axis  $a$  versus the number of direct-adjoint iterations for the fifth (center) cylinder. (d) Variance of the passive scalar versus time  $t \in [0, T^F]$ .



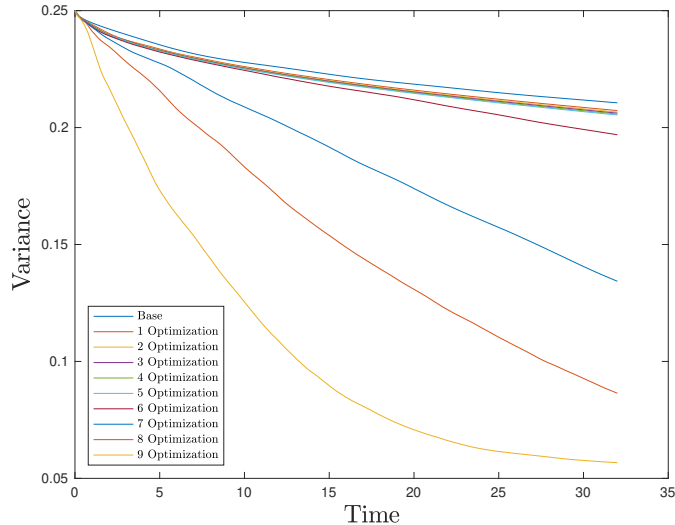


Figure 9: Case 3: mixing optimization using five stationary, rotating stirrers. Variance, as defined in equation (3), of the scalar field  $\theta$  versus time  $t \in [0, T^F]$ .

of the central stirrer (as suggested by the next adjoint step) would cause a collision with the other horizontally aligned stirrers.

#### 5.6. Case 4: one horizontally moving, rotating stirrer

All previous configurations relied on stationary stirrers, and thus only partially demonstrate the capabilities of the direct-adjoint method and the associated penalization framework. In this final case, we present a scenario that considers the optimization of the shape of a stirrer while being dragged through the binary fluid; the velocity of the stirrer is defined by a function of the form  $\cos(t)$ .

We neglect energy penalization (i.e.  $\lambda = 0$ ) in this case, as little effect is expected from a pure shape optimization, since the bulk of the energy expenditure is already contained in the back-and-forth motion of the stirrer.

We observe in figure 11 a pronounced decrease in the variance as the initially circular cylinder is lengthened vertically (for the position at  $t = 0$ ). The reason for this optimal configuration is certainly linked to the fact that dragging an elliptical stirrer across the interface starting in this vertical position achieves a great deal of mixing by producing small-scale structures. An alternative, initially horizontal design would perform significantly worse. In addition to this obvious observation, we notice that starting in the vertical position at  $t = 0$  allows the stirrer to take on the high-drag vertical position nine times during a full simulation cycles, while an initially horizontal ellipse would exhibit the same high-drag position only eight times per cycle. From the early stages of the cycle (e.g.  $t = 8$ ), we create a great many filamented structures that subsequently get diffused by the flow and help in ultimately producing a homogeneous mixture. This effect continues further throughout the simulation and leads to the substantial decrease in variance, as shown in figure 11.

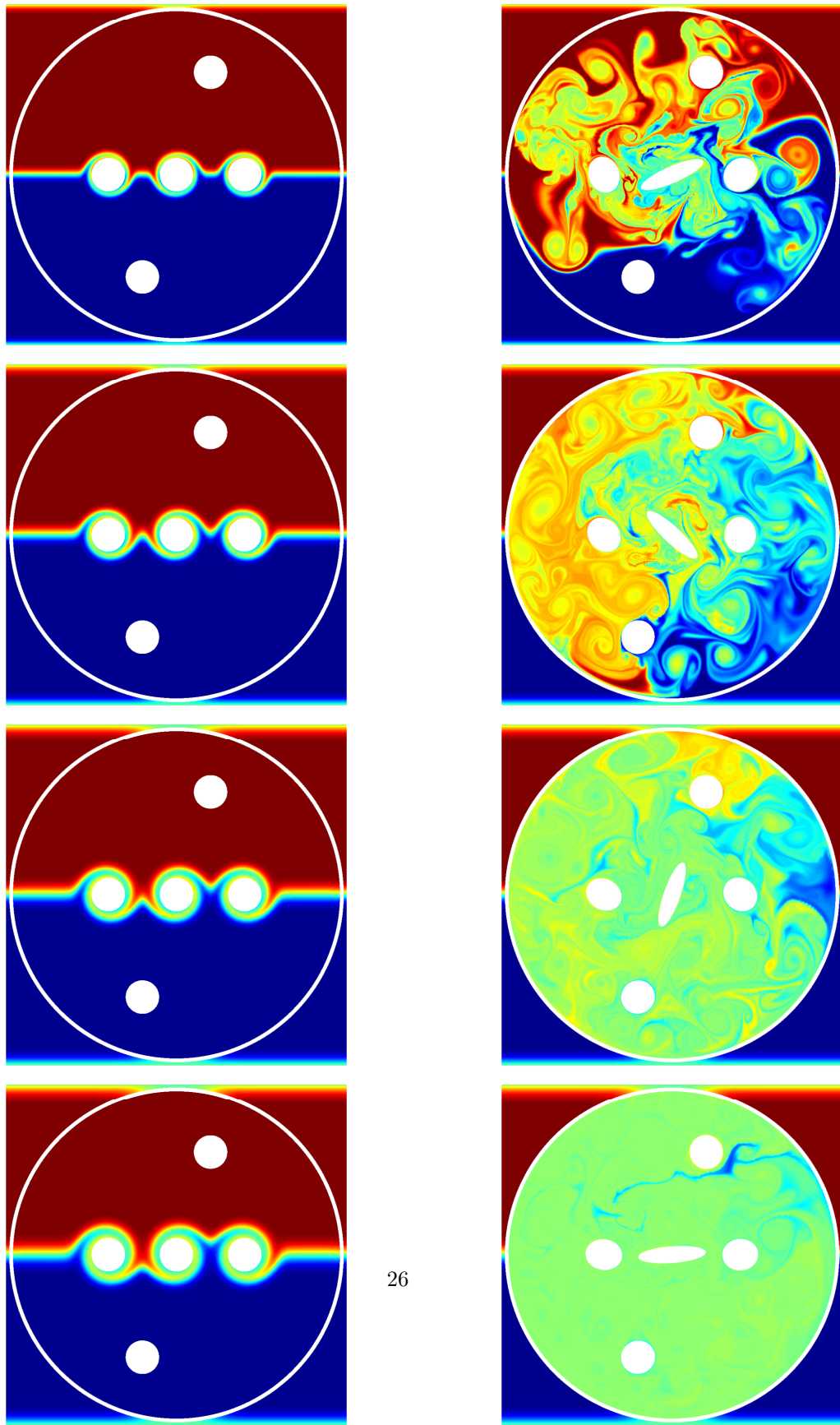


Figure 10: Case 3: mixing optimization using five stationary, rotating stirrers. Left column: unoptimized configuration, with snapshots at  $t = 8, 16, 24, 32$  (top to bottom). Right column: after seven direct-adjoint optimizations, with snapshots at  $t = 8, 16, 24, 32$  (top to bottom). For videos of these scenarios please refer to `5Before.mp4` and `5After.mp4`.

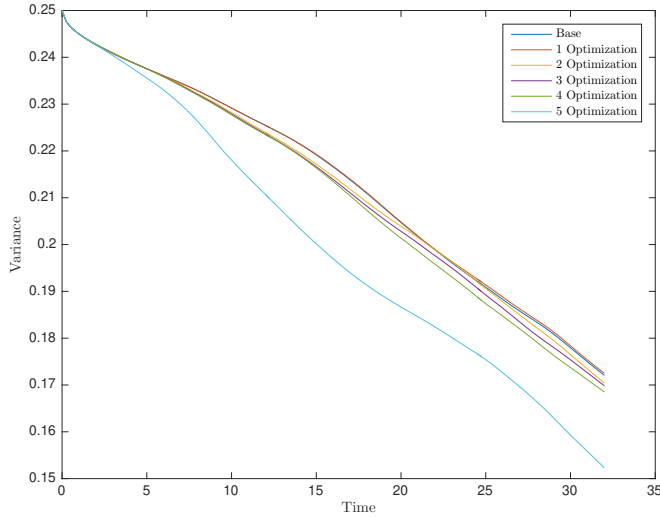


Figure 11: Case 4: mixing optimization using one horizontally moving, rotating stirrer. Variance, as defined in equation (3), of the scalar field  $\theta$  versus time  $t \in [0, T^F]$ .

Finally, we note that the direct-adjoint system, as introduced, is ignorant of the physical restrictions by the geometry; specifically, geometrically overlapping or otherwise colliding structures are not explicitly accounts for. For this reason, we have to manually terminate the optimization scheme in the case of such an event.

## 6. Conclusions

A computational framework has been presented that allows the efficient optimization of mixing strategies of binary fluids by moving stirrers. Among the control parameters for the optimization, the speed along a given path, the rotation speed of the stirrers and the geometry of the stirrers have been considered, but more complex setups are within the range of possibilities using the presented approach. The framework uses Brinkman penalization to embed and describe the stirrer elements and to track their interaction with the surrounding fluid. A resulting PDE-constrained optimization problem is then recast into a direct-adjoint (or primal-dual) formulation, which is subsequently solved iteratively, employing a checkpointing technique due the linkage of the direct and adjoint problem. Particular attention has been paid to the explicit formulation of path and shape gradients based on the penalized formulation. These gradients are then used to optimize the mixing efficiency (in our case, the variance of the passive scalar field), while observing the user-specified control-energy bounds.

Four test cases have illustrated the feasibility and flexibility of the presented approach: (i) the optimization of one simple stirrer, (ii) a double configuration, (iii) a layout with five stirrers, and (iv) a stirrer moving along user-specified path. In all cases, a significant improvement in mixing efficiency could be accomplished, and the optimization algorithm showed notable robustness in finding a more optimal solution.

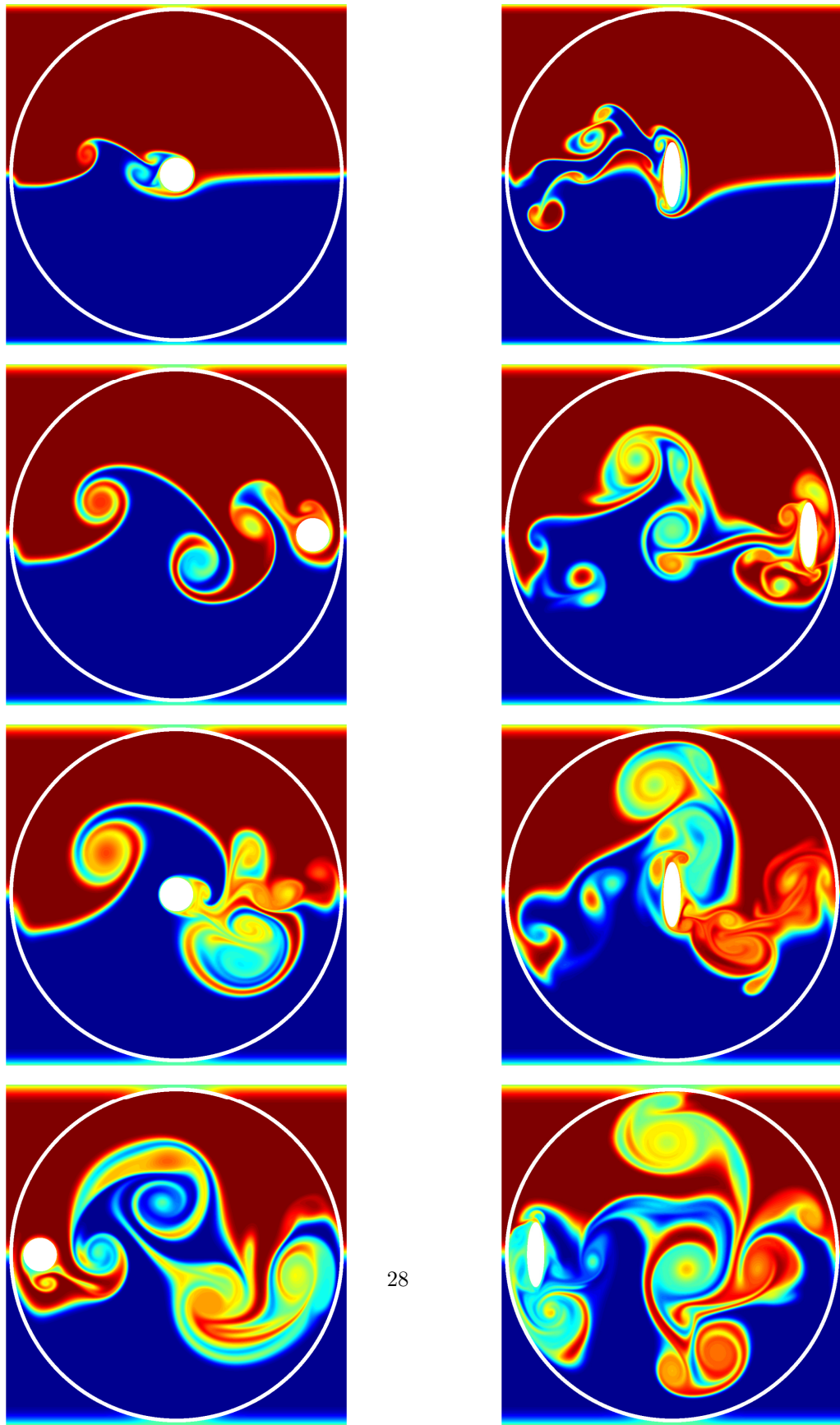


Figure 12: Case 4: mixing optimization using one horizontally moving, rotating stirrer. Left column: unoptimized configuration, with snapshots at  $t = 8, 16, 24, 32$  (top to bottom). Right column: after five direct-adjoint optimizations, with snapshots at  $t = 8, 16, 24, 32$  (top to bottom). For videos of these scenarios please refer to `CosBefore.mp4`

Despite these promising results, a few challenges remain. As is the case for any gradient-based optimization applied to a non-convex problem, only a local minimum can be guaranteed by our algorithm. User input (as was the case in setup (ii) in the text) is required to nudge the convergence towards a global optimum. This nudging could be accomplished more objectively by coupling the above algorithm to an annealing-type stochastic algorithm; approaches in this direction will be pursued in a future effort. Furthermore, the algorithm will be tested in a multi-parameter environment where a far larger control space (larger than the one considered here) will be treated; in particular, the convergence behavior will be monitored in this case, and methods, such as control-space splitting, will be investigated as means to accelerate convergence. Finally, three-dimensional layouts will be considered. The code is highly parallelized and scales well to many cores; good performance for large-scale optimizations of binary mixing problems is thus expected.

## Acknowledgements

We wish to thank the Research Computing Service at Imperial College London for providing the resources and support for this research.

## Appendix A. Arithmetic with Hadamard products

For the sake of clarity and completeness, we will give a brief summary of rules and relations involving the Hadamard product which has been used in the formulation of the governing equations and the derivation of the adjoint equations, and has produced a compact formalism and notation. In particular, we will consider the steps involved in the transfer of operators acting on the direct flow variables (such as velocities, pressure or passive scalar) onto corresponding operators acting on their adjoint equivalents. While this transfer is rather straightforward in the matrix-product case, care has to be exercised when the operator involves Hadamard products.

The Hadamard product, denoted by  $\circ$ , of two vectors  $\mathbf{a}$  and  $\mathbf{b}$  of identical size is defined as

$$\mathbf{c} = \mathbf{a} \circ \mathbf{b} = \mathbf{b} \circ \mathbf{a} \quad \text{with} \quad c_i = a_i b_i. \quad (\text{A.1})$$

It is defined as the element-wise product of two vectors and results in a vector  $\mathbf{c}$  equal in size to  $\mathbf{a}$  or  $\mathbf{b}$ .

It will be convenient to re-express the Hadamard product of two vectors in terms of a standard matrix product. To this end, we introduce the notation  $\mathbf{a}^{(D)}$  to indicate a diagonal matrix with the elements of  $\mathbf{a}$  along its main diagonal. With this notation we can restate the Hadamard product as

$$\mathbf{c} = \mathbf{a} \circ \mathbf{b} = \mathbf{a}^{(D)} \mathbf{b} = \mathbf{a} \mathbf{b}^{(D)}. \quad (\text{A.2})$$

In the derivation of the adjoint equations, we are faced with terms of the form

$$\mathcal{I} = \mathbf{a}^H (\mathbf{b} \circ [\mathbf{M}\mathbf{c}]). \quad (\text{A.3})$$

Expressions of this type constitute an inner product  $\mathcal{I}$  and arise from the nonlinear terms of the governing equations related to convective transport, but terms linked to the mask function can also yield the above example. They appear in the augmented Lagrangian formulation of the optimization problem. Due to our spatial discretization,  $\mathbf{a}$ ,  $\mathbf{b}$  and  $\mathbf{c}$  are column vectors of size  $n \times 1$  with  $n$  as

the total number of degrees of freedom, and  $\mathbf{M}$  is an  $n \times n$  matrix. During the derivation of the adjoint equations, the vector  $\mathbf{c}$  may represent a first variation of a flow variable, while the vector  $\mathbf{a}$  stands for the adjoint variable (see the main text for details). We seek to isolate this first variation (the vector  $\mathbf{c}$ ) by transferring all operators acting on it onto the adjoint variable represented by  $\mathbf{a}$  while preserving the inner product. Using the alternative formulation of the Hadamard product based on diagonal matrices, we obtain

$$\mathbf{a}^H (\mathbf{b} \circ [\mathbf{M}\mathbf{c}]) = \mathbf{a}^H (\mathbf{b}^{(D)}\mathbf{M}\mathbf{c}), \quad (\text{A.4a})$$

$$= \mathbf{a}^H \left( (\mathbf{M}^H \mathbf{b}^{(D)})^H \mathbf{c} \right), \quad (\text{A.4b})$$

$$= (\mathbf{M}^H \mathbf{b}^{(D)} \mathbf{a})^H \mathbf{c}, \quad (\text{A.4c})$$

$$= (\mathbf{M}^H [\mathbf{b} \circ \mathbf{a}])^H \mathbf{c}. \quad (\text{A.4d})$$

Using this simple rule we are able to efficiently manipulate most expressions in our adjoint derivations. We note that in the case of  $\mathbf{M}$  being an identity matrix, our relation simply reduces to

$$\mathbf{a}^H (\mathbf{b} \circ \mathbf{c}) = (\mathbf{b} \circ \mathbf{a})^H \mathbf{c} = (\mathbf{a}^H \circ \mathbf{b}^H) \mathbf{c}. \quad (\text{A.5})$$

## Appendix B. Explicit $\chi^\dagger$ -derivation

As a representative example of the full adjoint derivation, we will more explicitly perform the steps to arrive at the expression for the adjoint mask function  $\chi^\dagger$ , i.e., equation (20). These steps are illustrative of the remaining part of the adjoint formalism and involve the critical concepts that also apply to the momentum equations. The formulation as a spatially discretized problem, the incorporation of the boundary conditions via penalization and the use of Hadamard products to describe nonlinear terms aid in making the derivation less unwieldy and error-prone as in attempts on the continuous equations.

The expression for  $\chi^\dagger$  results, as an optimality condition, from a first variation of the augmented Lagrangian with respect to the mask functions  $\chi$ . We have

$$\begin{aligned}
\int_0^{T^F} \left( \frac{\partial \mathcal{L}}{\partial \chi_i} \right) \delta \chi_i dt &= \int_0^{T^F} \left( \frac{\partial \mathcal{J}}{\partial \chi_i} \right) \delta \chi_i dt \\
&- \int_0^{T^F} \mathbf{u}_j^{\dagger, H} \frac{\delta \chi_i}{C_\eta} \circ \mathbf{u}_j - \mathbf{u}_j^{\dagger, H} \frac{\delta \chi_i}{C_\eta} \circ (\mathbf{u}_{s,i})_j dt \\
&- \int_0^{T^F} p^{\dagger, H} \mathbf{A}_j \left[ \frac{\delta \chi_i}{C_\eta} \circ \mathbf{u}_j - \frac{\delta \chi_i}{C_\eta} \circ (\mathbf{u}_{s,i})_j \right] dt \\
&- \int_0^{T^F} \theta^{\dagger, H} \left[ -\delta \chi_i \circ \mathbf{u}_j \circ [\mathbf{A}_j \theta] + \delta \chi_i \circ (\mathbf{u}_{s,i})_j \circ [\mathbf{A}_j \theta] \right. \\
&\quad \left. - \mathbf{A}_j \left( [Pe^{-1}(-\delta \chi_i) + \kappa \delta \chi_i] \circ \mathbf{A}_j \theta \right) \right] dt \\
&- \int_0^{T^F} \chi_i^{\dagger, H} \delta \chi_i dt. \tag{B.1}
\end{aligned}$$

The task is to isolate the first variation  $\delta \chi_i$  from all terms and transfer any operator acting on it to act on the remaining terms. In this effort, we take advantage of the relation for the Hadamard product, explained in the previous appendix. Continuing from above, we obtain

$$\begin{aligned}
&= \lambda \int_0^{T^F} ((\mathbf{u}_{s,i})_j \circ \delta \chi_i)^H \mathbf{R}_i((\mathbf{u}_{s,i})_j \circ \chi_i) + ((\mathbf{u}_{s,i})_j \circ \chi_i)^H \mathbf{R}_i((\mathbf{u}_{s,i})_j \circ \delta \chi_i) dt \\
&- \int_0^{T^F} \frac{\mathbf{u}_j^{\dagger, H} \circ \mathbf{u}_j^H - \mathbf{u}_j^{\dagger, H} \circ (\mathbf{u}_{s,i})_j^H}{C_\eta} \delta \chi_i dt \\
&- \int_0^{T^F} \left[ \frac{[\mathbf{A}_j^H p^\dagger]^H \circ \mathbf{u}_j^H - [\mathbf{A}_j^H p^\dagger]^H \circ (\mathbf{u}_{s,i})_j^H}{C_\eta} \right] \delta \chi_i dt \\
&- \int_0^{T^F} \left[ -\theta^{\dagger, H} \circ (\mathbf{u}_j \circ [\mathbf{A}_j \theta])^H \delta \chi_i + \theta^{\dagger, H} \circ \left( (\mathbf{u}_{s,i})_j \circ [\mathbf{A}_j \theta] \right)^H \delta \chi_i \right. \\
&\quad \left. - [\mathbf{A}_j^H \theta^\dagger]^H [Pe^{-1}(-\delta \chi_i) + \kappa \delta \chi_i] \circ \mathbf{A}_j \theta \right] dt \\
&- \int_0^{T^F} \chi_i^{\dagger, H} \delta \chi_i dt. \tag{B.2}
\end{aligned}$$

Next, we collect matching terms and gather them under a single integral. We thus get

$$\begin{aligned}
&= \int_0^{T^F} \left( [2\lambda R_i((\mathbf{u}_{s,i})_j \circ \chi_i)] \circ (\mathbf{u}_{s,i})_j \right. \\
&\quad \left. - \frac{\mathbf{u}_j^\dagger \circ (\mathbf{u}_j - (\mathbf{u}_{s,i})_j) + [\mathbf{A}_j^H \mathbf{p}^\dagger] \circ (\mathbf{u}_j - (\mathbf{u}_{s,i})_j)}{C_\eta} \right. \\
&\quad \left. + \theta^\dagger \circ (\mathbf{u}_j \circ [\mathbf{A}_j \theta]) - \theta^\dagger \circ ((\mathbf{u}_{s,i})_j \circ [\mathbf{A}_j \theta]) \right. \\
&\quad \left. + (\kappa - Pe^{-1}) [\mathbf{A}_j^H \theta^\dagger \circ \mathbf{A}_j \theta] - \chi_i^\dagger \right)^H \delta \chi_i \, dt \tag{B.3}
\end{aligned}$$

We recall that this integral is identically zero, which implies that the integrand must vanish. We are then able to explicitly express  $\chi_i^\dagger$  in terms of our other variables; we obtain

$$\begin{aligned}
\chi_i^\dagger &= [2\lambda R_i((\mathbf{u}_{s,i})_j \circ \chi_i)] \circ (\mathbf{u}_{s,i})_j \\
&\quad - \frac{\mathbf{u}_j^\dagger \circ (\mathbf{u}_j - (\mathbf{u}_{s,i})_j) + [\mathbf{A}_j^H \mathbf{p}^\dagger] \circ (\mathbf{u}_j - (\mathbf{u}_{s,i})_j)}{C_\eta} \\
&\quad + (\theta^\dagger \circ [\mathbf{A}_j \theta]) \circ (\mathbf{u}_j - (\mathbf{u}_{s,i})_j). \tag{B.4}
\end{aligned}$$

Some simple manipulations leave us with the result from the main text,

$$\begin{aligned}
\chi_i^\dagger &= [2\lambda R_i((\mathbf{u}_{s,i})_j \circ \chi_i)] \circ (\mathbf{u}_{s,i})_j + \left[ \theta^\dagger \circ [\mathbf{A}_j \theta] - \frac{\Pi_j^\dagger}{C_\eta} \right] \circ (\mathbf{u}_j - (\mathbf{u}_{s,i})_j) \\
&\quad + (\kappa - Pe^{-1}) \mathbf{A}_j^H \theta^\dagger \circ \mathbf{A}_j \theta. \tag{B.5}
\end{aligned}$$

The system of adjoint evolution equations, as well as other optimality conditions, are derived in an analogous manner.

## References

### References

- [1] F. Lekien, C. Coulliette, A. Mariano, E. Ryan, L. Shay, G. Haller, J. Marsden, Pollution release tied to invariant manifolds: A case study for the coast of Florida, *Physica D: Nonlinear Phenomena* 210 (1-2) (2005) 1–20.
- [2] G. Hunt, P. Linden, The fluid mechanics of natural ventilation – displacement ventilation by buoyancy-driven flows assisted by wind, *Buildg. and Environm.* 34 (6) (1999) 707–720.
- [3] P. Linden, The fluid mechanics of natural ventilation, *Annu. Rev. Fluid Mech.* 31 (1) (1999) 201–238.
- [4] A. Annaswamy, A. Ghoniem, Active control in combustion systems, *IEEE Contr. Sys.* 15 (6) (1995) 49–63.



- [5] V. Hessel, H. Löwe, F. Schönfeld, Micromixers – a review on passive and active mixing principles, in: *Chemical Engineering Sciences*, Vol. 60, 2005, pp. 2479–2501.
- [6] N.-T. Nguyen, Z. Wu, Micromixers – a review, *J. Micromech. Microeng.* 15 (2) (2005) R1–R16.
- [7] H. Aref, Stirring by chaotic advection, *J. Fluid Mech.* 143 (1) (1984) 1–21.
- [8] C. Mattiussi, The finite volume, finite element, and finite difference methods as numerical methods for physical field problems, *Adv. Imag. and Elec. Phys.* 113 (2000) 1–146.
- [9] M. Glowinski, T. Pan, R. Wells Jr., X. Zhou, Wavelet and finite element solutions for the Neumann problem using fictitious domains, *J. Comp. Phys.* 126 (1) (1996) 40–51.
- [10] E. Arquis, J. Caltagirone, Sur les conditions hydrodynamiques au voisinage d’une interface milieu fluide-milieu poreux: application à la convection naturelle, *C.R. Acad. Sci. Paris II* 299 (1984) 1–4.
- [11] P. Angot, C.-H. Bruneau, P. Fabrie, A penalization method to take into account obstacles in incompressible viscous flows, *Num. Math.* 81 (4) (1999) 497–520.
- [12] Q. Liu, O. Vasilyev, A Brinkman penalization method for compressible flows in complex geometries, *J. Comp. Phys.* 227 (2) (2007) 946–966.
- [13] O. Boiron, G. Chiavassa, R. Donat, A high-resolution penalization method for large Mach number flows in the presence of obstacles, *Comp. & Fluids* 38 (3) (2009) 703–714.
- [14] N. Kevlahan, J.-M. Ghidaglia, Computation of turbulent flow past an array of cylinders using a spectral method with Brinkman penalization, *Eur. J. Mech. B/Fluids* 20 (3) (2001) 333–350.
- [15] F. Chantalat, C.-H. Bruneau, C. Galusinski, A. Iollo, Level-set, penalization and Cartesian meshes: A paradigm for inverse problems and optimal design, *J. Comp. Phys.* 228 (17) (2009) 6291–6315.
- [16] C.-H. Bruneau, F. Chantalat, A. Iollo, B. Jordi, I. Mortazavi, Modelling and shape optimization of an actuator, *Struct. Multidisc. Optim.* 48 (6) (2013) 1143–1151.
- [17] M. Juniper, Optimization with nonlinear adjoint looping, in: *Int. Workshop on Nonnormal and Nonlinear Effects in Aero- and Thermoacoustics*, Munich, Germany, 2010.
- [18] D. D’Alessandro, M. Dahleh, I. Mezic, Control of mixing in fluid flow: a maximum entropy approach, *IEEE Trans. Autom. Contr.* 44 (10) (1999) 1852–1863.
- [19] G. Mathew, I. Mezic, S. Grivopoulos, U. Vaidya, L. Petzold, Optimal control of mixing in Stokes fluid flows, *J. Fluid Mech.* 580 (2007) 261–281.
- [20] Z. Lin, J.-L. Thiffeault, C. Doering, Optimal stirring strategies for passive scalar mixing, *J. Fluid Mech.* 675 (2011) 465–476.
- [21] J. Ottino, Mixing, chaotic advection, and turbulence, *Annu. Rev. Fluid Mech.* 22 (1) (1990) 207–254.
- [22] J.-L. Thiffeault, Using multiscale norms to quantify mixing and transport, *Nonlinearity* 25 (2) (2012) R1.

- [23] R. Hemrajani, G. Tatterson, *Mechanically Stirred Vessels*, John Wiley & Sons, Inc., 2004, pp. 345–390.
- [24] E. Paul, V. Atiemo-obeng, S. Kresta, *Frontmatter*, John Wiley & Sons, Inc., 2004, pp. i–lxi.
- [25] G. Mathew, I. Mezić, L. Petzold, A multiscale measure for mixing, *Physica D: Nonlinear Phenomena* 211 (1–2) (2005) 23–46.
- [26] D. Foures, C. Caulfield, P. Schmid, Localization of flow structures using  $\infty$ -norm optimization, *J. Fluid Mech.* 729 (2013) 672–701.
- [27] K. Schneider, Numerical simulation of the transient flow behaviour in chemical reactors using a penalisation method, *Comp. & Fluids* 34 (10) (2005) 1223–1238.
- [28] T. Engels, D. Kolomenskiy, K. Schneider, J. Sesterhenn, FluSI: A novel parallel simulation tool for flapping insect flight using a fourier method with volume penalization, *SIAM J. Sci. Comp.* (2015) 1–21.
- [29] B. Kadoch, D. Kolomenskiy, P. Angot, K. Schneider, A volume penalization method for incompressible flows and scalar advection-diffusion with moving obstacles, *J. Comp. Phys.* 231 (12) (2012) 4365–4383.
- [30] R. Horn, C. Johnson, *Matrix Analysis*, 2nd Edition, Cambridge University Press, New York, NY, USA, 2012.
- [31] T. Hou, R. Li, Computing nearly singular solutions using pseudo-spectral methods, *J. Comp. Phys.* 226 (2007) 379–397.
- [32] D. Kolomenskiy, K. Schneider, A Fourier spectral method for the Navier-Stokes equations with volume penalization for moving solid obstacles, *J. Comp. Phys.* 228 (16) (2009) 5687–5709.
- [33] D. Foures, C. Caulfield, P. Schmid, Optimal mixing in two-dimensional plane Poiseuille flow at finite Péclet number, *J. Fluid Mech.* 748 (2014) 241–277.